# Thermohydraulic performance of microchannel heat sinks with triangular ribs on sidewalls – Part 1: local fluid flow and heat transfer characteristics

Lei Chai[a, *], Liang Wang[b], Xin Bai[c]

[a] RCUK National Centre for Sustainable Energy Use in Food Chain (CSEF), Brunel University London, Uxbridge, Middlesex UB8 3PH, UK

[b] Institute of Engineering Thermophysics, Chinese Academy of Sciences, Beijing 100190, China

[c] Advanced Sustainable Manufacturing Technologies (ASTUTE 2020), College of Engineering, Swansea University, Swansea SA1 8EN, UK

**Abstract** Triangular ribs are mounted on the parallel sidewalls of microchannels in order to reinitialize the thermal boundary layer and improve the mixing of cold and hot fluids. This paper presents a detailed numerical study on local laminar fluid flow and heat transfer characteristics in microchannel heat sinks with tandem triangular ribs for Reynolds number of 443. Three-dimensional conjugate heat transfer models considering entrance effect, viscous heating, as well as temperature-dependent thermophysical properties are employed. Water and silicon are respectively used as fluid and solid for the computational domain. Triangular ribs are attached in microchannels with either aligned or offset arrangement. Four non-dimensional geometry parameters relative to the width, height, converging-diverging ratio and spacing of triangular ribs are proposed to investigate the influence on local fluid flow and heat transfer characteristics. Velocity contour, pressure and temperature distributions are examined to demonstrate the basic fluid flow and heat transfer mechanism. Local pressure and temperature profiles are studied to show the influence of the triangular ribs on fluid flow and heat transfer process. Local friction factor and Nusselt number for different non-dimensional geometry variables are further investigated to comprehensively indicate the impact of triangular ribs. Results shows that

[*] Corresponding author. Tel.: +44 (0)1895 265834.

E-mail address: Lei.Chai@brunel.ac.uk (Lei Chai).

the triangular ribs can significantly reduce the temperature rise of the heat sink base and efficiently prevent the drop of local heat transfer coefficient along the flow direction, but also result in higher local friction factor than the straight microchannel. For the studied operation conditions and geometry parameters of flow passage, the heat sink base temperature varies in the range of from 301.90 to 324.31 K, the computed pressure drop and heat transfer coefficient fluctuate from one triangular rib to the next and their amplitude and wavelength significantly depend on the geometry and arrangement of triangular ribs. Compared to the reference straight microchannel heat sink, a superior configuration considered in this paper can yield an improvement of up to 2.15 times higher of average Nusselt number.

**Key words** microchannel heat sink; triangular rib; geometry parameter; local thermohydraulic characteristics

## 1. Introduction

With the rapid development of microminiaturization technology and the urgent requirement of high heat flux dissipation, microchannel heat sink incorporating single-phase liquid flow has been widely applied in a variety of applications, such as the cooling of electronic device, laser process equipment and aerospace technology, etc. Firstly proposed by Tuckerman and Pease [1] in the early 1980s, it has many advantages, such as compactness, light weight and higher heat transfer surface area to fluid volume ratio compared with other macroscale heat exchangers. And extensive studies have been conducted on the fluid flow and heat transfer characteristics in microchannel heat sinks. Furthermore, the highly-integrated electronic circuit has increased the heat flux in electronic chips up to 1 $kW/cm^2$, pushing the traditional straight microchannel heat sink to its thermal limit [2, 3]. Recently, many significant works, based on passive techniques for heat transfer augmentation, have been conducted with the potential to deliver more high heat flux for microelectronic

applications [4].

For the interrupted microchannel heat sink, Xu et al. [5, 6] demonstrated a heat sink consisted of a set of separated zones adjoining shortened parallel microchannels and transverse microchambers. Results showed that the hydraulic and thermal boundary layers were redeveloped in each separated zone, and the periodic thermal developing flow resulted in significant heat transfer enhancement and similar or reduced pressure drop. The pressure drop was attributed to two effects, one was the pressure recovery effect when liquids left the upstream zone and the other was the increased head loss once liquid entered the next zone. Chai et al. [7, 8, 9] and Wong and Lee [10] introduced the staggered ribs into the transverse microchambers. They found that the staggered ribs not only suppressed the heat transfer deterioration in the microchamber region, but also improved the heat transfer coefficient to a much higher level in the separated microchannel zone, leading to further improved heat transfer performance due to better flow separation and mixing of hot and cold liquids. The local pressure drop and heat transfer in the microchamber were mainly influenced by Bernoulli effect, entrance and exit geometry, and the developed stagnation or recirculation zone.

For the microchannel heat sink with passive microstructures, Promvonge et al. [11] examined the laminar flow and heat transfer characteristics of a three-dimensional isothermal square channel with 45$^{o}$-angled baffles mounted in tandem with both inline and staggered arrangements on the lower and upper walls. In each of the main vortex flows, a pair of stream wise twisted vortex flows was created by the baffles, which induced impinging flows on a sidewall and wall of the baffle cavity and led to drastic increase in heat transfer rate than the reference smooth channel. Liu et al. [12] and Ebrahimi et al. [13] investigated the thermohydraulic performance of a microchannel heat sink with longitudinal vortex generators (LVG). Due to the better fluid mixing, reducing the thermal boundary-layer thickness and an increase of the heat transfer area, the microchannel with LVG can enhance heat transfer while consuming larger pressure drop, compared with the

smooth microchannel. Foong et al. [14] studied the fluid flow and heat transfer characteristics of a square microchannel with four longitudinal internal fins. Parametric study on thermal performance showed that for a given microchannel, there was an optimal fin height that provided the best possible heat transfer and pressure drop characteristics. Compared to a smooth microchannel, the microchannel with internal longitudinal fins had the following beneficial features: shorter length required for the development of the thermal boundary layer, better flow mixing, steeper velocity gradient at the heated surface, increase of surface area for heat transfer, and increase in surface heat transfer coefficient and Nusselt number. Xie et al. [15] investigated the thermal and fluid flow characteristics of microchannel heat sinks with internal vertical Y-shaped bifurcations and examined the effect of the length of Y-shaped bifurcation and the angles of the arms on the overall performance. The longest internal Y-shaped bifurcation microchannel resulted in the best thermal performance, and a larger arm angle led to better thermal performance but larger pressure drop.

For the microchannel heat sink with periodically varying cross-sections, Sui et al. [16, 17], Mohammed et al. [18] and Lin et al. [19] studied the laminar flow and heat transfer in wavy microchannel heat sinks. When the liquid passed through the wavy microchannels, secondary flow was generated, and the quantity and the location of the vortices can change along the flow direction and result in chaotic advection, which can greatly enhance the convective mixing of the flow. The penalty of pressure drop in the wavy microchannels can be less significant than the heat transfer enhancement. And the increase of relative wavy amplitude can result in better heat transfer performance. Ghaedamini et al. [20] studied the effects of geometrical configuration (aspect ratio, waviness, and expansion factor) on heat transfer and fluid flow in a converging–diverging microchannel heat sink. For the regular advection regime, increasing the waviness resulted in better heat transfer performance, while for the chaotic advection regime, heat transfer increased drastically albeit with a higher pressure drop penalty. Furthermore, the counter rotating vortices created in the trough region were

found to have an adverse effect on the performance of heat transfer. Chai et al. [21, 22] and Xia et al. [23, 24] investigated the fluid flow and heat transfer in microchannel heat sinks with fan-shaped or triangular reentrant cavities on sidewalls. The effects of geometry parameters, including the length, width, height and spacing of the reentrant cavity, on pressure drop and heat transfer were further studied. The heat transfer enhancement mechanism was attributed to the interruption of boundary layer formation, the enhanced convective fluid mixing, the increased heat transfer surface area and the jet and throttling effects caused by the altered flow passage. Chai et al. [25-28] studied the thermohydraulic performance of microchannel heat sinks with aligned or offset fan-shaped ribs on sidewalls and investigated the effects of geometry parameters (length, width, height, spacing and arrangement of fan-shaped rib) in such microchannel heat sinks. Local heat transfer performance showed that the mounted fan-shaped ribs on sidewall can effectively prevent the decline of local heat transfer coefficient along the flow direction, and the geometric parameters of ribs had a significant influence on the performance of such microchannel heat sinks. For further heat transfer augmentation, Xia et al. [29, 30, 31] and Ghani et al. [32] mounted the rectangular ribs into the microchannels with periodically varying cross-sections and investigated their thermohydraulic performance. The combined effect of cavity and rib was found to give better heat transfer performance than using individual technique. The heat transfer mechanism can be attributed to the interruption of thermal boundary layer, the enhancement of internal disturbance, the larger heat transfer area and the elimination of the stagnation zone in the cavity.

From the above investigations, it can be observed that the microchannel heat sink with passive techniques can result in much better heat transfer performance, but is generally accompanied by larger pressure drop penalty, and the geometry parameters of passive structures have significant influence on the thermohydraulic performance of heat sink. For the microchannel heat sink with aligned or offset ribs on sidewalls, Chai et al. [25] has conducted three-dimensional numerical models with five different shapes of offset ribs to examine

the local and average friction factor, and further for a systematic and detailed analysis, Chai et al. [26, 27, 28] concentrated on the fan-shaped ribs and investigated the influence of rib geometry and arrangement on thermal and hydraulic characteristics of such microchannel heat sink. As a continuous study, this paper focus on the triangular ribs mounted in microchannels with either aligned or offset arrangements. Four non-dimensional geometry variables relative to the width, height, converging-diverging ratio and spacing are designed. The purpose of the first part of a two-part study is to supply the basic fluid flow and heat transfer mechanism in such microchannel heat sink and to identify the effects of the geometric and arrangement parameters on local fluid flow and heat transfer characteristics.

## 2. Model formulation and solution methodology

### *2.1. Geometry structure of microchannel*

In order to save the computation time and take advantage of symmetry, a control volume containing a single microchannel and its surrounding solid along with the base is selected for the numerical study, see Fig. 1a. The length ($L_{com}$), width ($W_{com}$) and height ($H_{com}$) of the computational domain are 10 mm, 0.25 mm and 0.35 mm, and the width ($W_c$) and height ($H_c$) of microchannel are 0.1 mm and 0.2 mm, respectively. The triangular ribs are mounted on the two parallel sidewalls in tandem for both aligned and offset arrangements. The geometric parameters of triangular ribs are shown in Fig. 1b, including the width ($W_r$), height ($H_r$), converging width ($W_{con}$) and spacing ($S_r$), and are used to determine four non-dimensional variables, including the width ratio of the rib to microchannel ($W_r/W_c$), ratio of the rib height to the microchannel width ($H_r/W_c$), width ratio of converging region to the single rib ($W_{con}/W_r$), and ratio of the rib spacing to the microchannel width ($S_r/W_c$). Moreover, a typical straight microchannel heat sink without ribs is introduced for comparison.

*2.2. Numerical model*

A three-dimensional solid-fluid conjugate heat transfer model has been developed by Chai et al. [25] with the assumptions of steady, developing laminar flow and considerations of temperature-dependent fluid thermophysical properties and viscous dissipation. The working fluid is water and the material of the heat sink is silicon. The continuity, momentum and energy equations for the problem can be written as

$$\frac{\partial}{\partial x_i}\left(\rho u_i\right)=0 \tag{1}$$

$$\frac{\partial}{\partial x_i}\left(\rho_{\mathrm{f}} u_i u_j\right)=-\frac{\partial p}{\partial x_j}+\frac{\partial}{\partial x_i}\left[\mu_{\mathrm{f}}\left(\frac{\partial u_j}{\partial x_i}+\frac{\partial u_i}{\partial x_j}\right)\right] \tag{2}$$

$$\frac{\partial}{\partial x_i}\left(\rho_{\mathrm{f}} u_i c_{\mathrm{pf}} T\right)=\frac{\partial}{\partial x_i}\left(k_{\mathrm{f}}\frac{\partial T}{\partial x_i}\right)+\mu_{\mathrm{f}}\left[2\left(\frac{\partial u_i}{\partial x_i}\right)^2+\left(\frac{\partial u_j}{\partial x_i}+\frac{\partial u_i}{\partial x_j}\right)^2\right] \tag{3}$$

The heat conduction equation in the heat sink base is

$$\frac{\partial}{\partial x_i}\left(k_{\mathrm{s}}\frac{\partial T}{\partial x_i}\right)=0 \tag{4}$$

where $x_1$, $x_2$ and $x_3$ are $x$, $y$ and $z$ coordinates, respectively, as shown in Fig. 1a, $u$ is the fluid velocity vector, $p$ is the hydrodynamic pressure, $\rho_{\mathrm{f}}$, $\mu_{\mathrm{f}}$, $c_{\mathrm{pf}}$ and $k_{\mathrm{f}}$ are the water density, dynamic viscosity, specific heat capacity and thermal conductivity, respectively, and their temperature-dependent property equations are listed in Table 1 [33]. $k_{\mathrm{s}}$ is the thermal conductivity of silicon and is set 148 $\mathrm{W\cdot m^{-1}\,K^{-1}}$ for the computation.

For the sake of completeness, the boundary conditions corresponding to Fig.1a are mathematically illustrated in Table 2. The inlet flow velocity $u_{\mathrm{in}}$ is selected to make sure the average velocity ($\bar{u}$) in the constant cross-section region is 3 $\mathrm{m\cdot s^{-1}}$ and the corresponding Reynolds number (*Re*) is 443, and $T_{\mathrm{in}}$ = 293 K is set as the given temperature at the channel inlet. At the channel outlet, a constant pressure boundary condition $p_{\mathrm{out}}$ = 0 (gauge pressure) is applied. At the base of computational domain, a constant heat flux of $q_{\mathrm{w}}$ = $10^6$ $\mathrm{W\cdot m^{-2}}$ is employed. At the two sides of the computational domain, zero normal velocity and zero normal gradient of temperature for the symmetry planes. And for other surfaces, adiabatic boundary is

applied.

The CFD software ANSYS FLUENT 12.0 was sued to solve the governing equations. The SIMPLEC algorithm is applied to solve the governing differential equations for the velocity, pressure and temperature fields in the control volume. The convergence criteria is set with the normalized residuals of momentum and energy equations at $10^{-5}$ for all variables. For every microchannel, a grid independence test is performed using several different mesh sizes. The grid independence test is similar to Chai et al. [25]. For example, for the microchannel heat sink ($W_r$ = 0.1 mm, $H_r$ = 0.25 mm, $S_r$ = 0.4 mm and $W_{con}$ = 0.07 mm, offset arrangement), various meshes with number of cells ranging from 0.293 to 1.123 million are tested. The indicators of thermohydraulic performance are insensitive to further grid refinement (with maximum deviations of 0.52% for friction factor, 0.85% for Nusselt number) beyond a mesh of about 0.703 millions, which is used in the present study. Comparison of numerical results with the experimental results from Chai et al. [24] as shown in Fig. 2 further ensures the accuracy and reliability of numerical code.

## 3. Data acquisition

Reynolds number is defined as

$$Re = \frac{\rho_f \bar{u} D_h}{\mu_f} \tag{14}$$

where $\rho_f$ is the volume average fluid density, $\bar{u}$ is the average flow velocity as mentioned above, $D_h$ is the hydraulic diameter calculated based on the constant cross-section region, $\mu_f$ is the mass average fluid dynamic viscosity. The $\rho_f$ and $\mu_f$ are defined as

$$\rho_f = \frac{\int \rho_{f,i} dV}{V} \tag{15}$$

$$\mu_f = \frac{\int \mu_{f,i} \rho_{f,i} dV}{\int \rho_{f,i} dV} \tag{16}$$

Local and average Fanning friction factor is calculated by

$$f_x = \frac{(p_{in} - p_x)D_h}{2\rho_f (x - x_{in}){u_m}^2} \tag{17}$$

$$\overline{f} = \frac{(p_{in} - p_{out})D_h}{2\rho_f L\overline{u}^2} \tag{18}$$

where $L$ is the length of computational domain, $p_{in}$ is the mass-weighted average pressure in the channel inlet and $p_{out}$ is the pressure in the channel outlet. The $p_x$ is defined as

$$p_x = \frac{\int p_{x,i}\rho_{f,i}\left|\vec{u}\cdot d\vec{A}\right|}{\int \rho_{f,i}\left|\vec{u}\cdot d\vec{A}\right|} \tag{19}$$

The $p_{in}$ is defined as

$$p_{in} = \frac{\int p_{in,i}\rho_{f,i}\left|\vec{u}\cdot d\vec{A}\right|}{\int \rho_{f,i}\left|\vec{u}\cdot d\vec{A}\right|} \tag{20}$$

Local and average heat transfer coefficient and Nusselt number are calculated by

$$h_x = \frac{q_w LW}{A(T_{w,x} - T_{f,x})} \tag{21}$$

$$\overline{h} = \frac{q_w LW}{A(\overline{T_w} - \overline{T_f})} \tag{22}$$

$$Nu_x = \frac{h_x D_h}{k_f} \tag{23}$$

$$\overline{Nu} = \frac{\overline{h}D_h}{k_f} \tag{24}$$

where $q_w$ represents the heat flux at the silicon base, $A$ is the contact surface area of water and silicon based on the straight microchannel, $W$ is the width of computational domain, $k_f$ is the mass average fluid thermal conductivity and defined as

$$k_f = \frac{\int k_{f,i}\rho_{f,i}dV}{\int \rho_{f,i}dV} \tag{25}$$

$T_{w,x}$ and $T_{f,x}$ are the local heat sink base temperature and the local bulk fluid temperature, respectively, defined as

$$T_{w,x} = \frac{\int T_{w,x,y}\, dy}{\int dy} \tag{26}$$

$$T_{f,x} = \frac{\int T_{f,i,x}\, \rho_{f,i,x} \left| \vec{v} \cdot d\vec{A} \right|}{\int \rho_{f,i,x} \left| \vec{v} \cdot d\vec{A} \right|} \tag{27}$$

## 4. Results and discussion

### *4.1. CFD plots of velocity, pressure and temperature distributions*

Figures 3, 4 and 5 respectively present the local velocity, pressure and temperature distributions with $x$ in the range of 6.0 to 6.8 mm in the plane of $z$ = 0.25 mm at $Re$ = 443 for different heat sinks, and Table 3 indicates the corresponding geometry parameters. As shown in Fig. 3, for the straight microchannel heat sink (MCHS), the largest magnitude of fluid velocity is observed at the center line while its slowest valves is observed at the walls, the flow profile's shape does not change, and there is no velocity fluctuation in the $y$ direction. The aligned triangular ribs result in the increase or decrease of fluid velocity due to the Bernoulli effect, and the MCHS-ATR shows the similar dynamic mechanism of the converging–diverging channel. The offset triangular ribs lead to the change of flow direction due to the asymmetric arrangement and make the MCHS-OTR performs the similar dynamic mechanism of the wavy channel. As mentioned above, both the converging–diverging channel and wavy channel can be beneficial for heat transfer by improvement of the convective fluid mixing, but their enhancement quality significantly depends on the channel geometry. The triangular ribs can also interrupt the development of thermal boundary layer due to the flow fluctuation near the walls. However, it should be noted that at the downstream of triangular ribs, the fluid velocity near the walls is very small and some recirculation regions are formed there, particularly for the MCHS-ATR. Depending on the intensity of the secondary flow, the recirculation can lead to improvement or deterioration of heat transfer. As shown in Fig. 3, the different rib geometry but the same arrangement can result in different

velocity distribution and extent of recirculation, which also have a significant influence on the thermohydraulic performance. As shown in Fig. 4, the pressure of the MCHS decreases continuously and steadily due to frictional losses along the channel, while the pressure drop of the microchannel with triangular ribs shows different patterns. The effect of aligned triangular ribs on pressure drop is mainly caused by the Bernoulli effect, where the pressure rapidly decreases with the converging flow passage, increases with the diverging flow passage which withdraws some pressure drop caused by fluid friction, and remains a slow increase in the constant cross-section region which results in the inverse pressure gradient. The effect of offset triangular ribs on pressure drop is mainly caused by the altered flow direction and partly by the changed flow passage. The developed wavy flow can extend the flow length and prevent the development of hydraulic boundary layer to cause more friction pressure drop. Regions with inverse pressure gradient is also found downstream of the offset triangular ribs, but its regime is much smaller than that caused by the aligned ones. Comparison of pressure distribution for the same geometry but different arrangement shows that the aligned triangular rib can cause much larger pressure drop than the offset ones. For the local temperature distribution as shown in Fig. 5, the large temperature gradient near the channel walls is obvious for the MCHS, indicating that the mixing of hot and cold fluid is very weak. The offset triangular ribs can effectively enhance the mixing of cold and hot fluid, which lead to lower temperature in the heat sink substrate and better heat transfer performance. The aligned triangular ribs do not perform as well as the offset ones due to the large temperature gradient at the downstream of ribs. Fig. 5 also shows the effects of different rib geometry but with the same arrangement on temperature distribution and heat transfer, where the MCHS-ATR1 and MCHS-OTR1 respectively show better performance than the MCHS-ATR2 and MCHS-OTR2.

*4.2. Effect of rib width on local fluid flow and heat transfer characteristics*

Figures 6a, 6b and 6c show the local pressure ($p_x$) along the flow direction and the corresponding Poiseuille number ($f_xRe$) with the non-dimensionalized length ($x^+ = x/(D_hRe)$) as $Re$ = 443. The tested geometry parameters are $W_r$ = 0.1, 0.2, 0.3 and 0.4 mm, $H_r$ = 0.025 mm, $W_{con}$ = 0.07 mm and $S_r$ = 0.4 mm. Compared with the MCHS, the channel with triangular ribs result in dramatic increase in the local pressure, particularly for the aligned arrangement. The $p_x$ at a given $x$ position is larger for $W_r/W_c$ = 1 and 4 than $W_r/W_c$ = 2 and 3, which is different from the pressure variation in the channel with fan-shaped ribs [27] where the $p_x$ increases with the increasing of $W_r$, indicating that different rib shapes lead to different fluid flow characteristics. As shown in Fig. 6b, the aligned triangular ribs result in larger pressure fluctuation with the changed flow passage than the offset ones, and the diverging flow passage with larger $W_r$ leads to more obvious inverse pressure gradient. As shown in Fig. 6c, the triangular ribs result in different local friction factor and Poiseuille number. For the MCHS, the $f_xRe$ declines quickly in the hydrodynamic developing region, and then decreases very slowly as $x^+ > 0.055$ due to the decreased viscosity. For the microchannel with triangular ribs, the $f_xRe$ at the channel inlet is much larger than that of the MCHS, resulting from the larger pressure gradient caused by the combined effect of the hydrodynamic developing flow with the converging of flow passage. And the $f_xRe$ presents a wave motion around a reference and the wave amplitude is much higher for MCHS-ATR than MCHS-OTR, and the wave amplitude becomes smaller along the flow direction partly with the flow development and partly by the definition of the local friction factor.

Figures 7a and 7b illustrate the effect of rib width on local heat transfer characteristic, respectively for $T_{w,x}$ and $Nu_x$ along the flow direction as $Re$ = 443, where the non-dimensionalized length $x^* = x/(D_hRePr)$. The triangular ribs can significantly reduce the temperature rise of the heat sink base along the flow direction and is thus invaluable for applications involving hot spots mitigation in the electronic devices. Along the whole length of microchannel, the $T_{w,x}$ is increased by 20.8 K for MCHS, but just 10.1, 9.9, 11.1 and 11.1 K

respectively for MCHS-ATR with $W_r/W_c$ = 1, 2, 3 and 4, and 9.9, 9.8, 11.5 and 12.2 K respectively for MCHS-OTR with $W_r/W_c$ = 1, 2, 3 and 4. As a result, the microchannel with triangular ribs efficiently prevents the drop of $Nu_x$. $Nu_x$ also shows a wave motion around a reference with the changed converging–diverging flow passage, where the converging flow passage leads to an increase of $Nu_x$ while the diverging one results in a decrease. The motion is more obvious for the MCHS-ATR than the MCHS-OTR due to the larger variation of flow passage. In addition, compared with the variation of $Nu_x$ with $W_r$ for the fan-shaped ribs [27], the triangular rib width shows greater influence on the local heat transfer performance. For $W_r/W_c$ from 1 to 4, the $Nu_x$ of channel with triangular ribs varies in the range of 9 to 12.5 while only 10 to 12 for the channel with fan-shaped ones.

*4.3. Effect of rib height on local fluid flow and heat transfer characteristics*

Figures 8 and 9 demonstrate the effect of $H_r$ on $p_x$ and $f_xRe$ as $Re$ = 443. The geometry parameter is $W_r$ = 0.1 and 0.2 mm, $W_{con}$ = 0.07 mm, $S_r$ = 0.4 mm and $H_r$ = 0.005, 0.01, 0.015, 0.02 and 0.025 mm. As $H_r/W_c$ = 0.05 and 0.1, the MCHS-ATR presents the similar $p_x$ at a specific position to the MCHS-OTR, and just a little higher than the MCHS, and without obvious pressure fluctuation along the changed flow passage. As $H_r/W_c$ = 0.15, 0.2 and 0.25, the MCHS-ATR shows much higher $p_x$ at a specific position than the MCHS-OTR and the difference of $p_x$ between them becomes much larger with increased $H_r$, and the $p_x$ of MCHS-ATR shows much larger pressure fluctuation than that of the MCHS-OTR. These results indicate that only the $H_r$ is large enough, does the rib exert an influence on the hydraulic boundary layer and trigger the pressure fluctuation. Corresponding to the $p_x$ along the flow direction, the variation of $f_xRe$ with $x^+$ could be identified: As $H_r/W_c$ = 0.05 and 0.1, the $f_xRe$ at a specific $x^+$ is almost similar for MCHS-ATR and MCHS-OTR and just a little higher than the MCHS, while as $H_r/W_c$ = 0.15, 0.2 and 0.25, the $f_xRe$ at a specific $x^+$ is much larger for

MCHS-ATR than MCHS-OTR and the difference becomes extremely larger with increase of $H_r/W_c$.

Figures 10 and 11 show the effect of $H_r$ on $T_{w,x}$ and $Nu_x$ as $Re$ = 443. $T_{w,x}$ at a specific position largely decreases with the increase of $H_r/W_c$, indicating a higher rib can effectively interrupt the thermal boundary layers and improve the heat transfer performance. With increase of $H_r$ from 0.005 to 0.025 mm, the $T_{w,x}$ of MCHS-ATR along the flow direction declines from 18.9 to 10.0 K as $W_r$ = 0.1 mm and from 19.9 to 9.9 K as $W_r$ = 0.2 mm, and that of MCHS-OTR drops from 19.1 to 9.9 K as $W_r$ = 0.1 mm and from 19.8 to 9.8 K as $W_r$ = 0.2 mm. As a result, the $Nu_x$ at a specific $x^*$ obviously increases with increased $H_r/W_c$, and a larger $H_r/W_c$ can keep the $Nu_x$ at a higher level along the flow direction. As $H_r/W_c$ = 0.05 and 0.1, the $Nu_x$ continually drops along the flow direction and does not show obvious fluctuation as water flows across the triangular ribs, while as $H_r/W_c$ = 0.2 and 0.25, the $Nu_x$ shows a much higher level for both MCHS-ATR and MCHS-OTR and the $Nu_x$ for MCHS-ATR shows clear fluctuation as water flows across the triangular ribs.

*4.4. Effect of rib's converging-diverging ratio on local fluid flow and heat transfer characteristics*

Figures. 12 and 13 show the effect of $W_{con}/W_r$ on $p_x$ and $f_xRe$ as $Re$ = 443 with the geometry parameter of $H_r$ = 0.025 mm, $S_r$ = 0.4 mm, $W_{con}$ = 0.01, 0.03, 0.05, 0.07 and 0.09 mm as $W_r$ = 0.1 mm and 0.02, 0.06, 0.1, 0.14 and 0.18 mm as $W_r$ = 0.2 mm. The $p_x$ at a specific position is generally higher for smaller or larger $W_{con}/W_r$ and lower for medium $W_{con}/W_r$, and changes much more with $W_{con}/W_r$ for MCHS-ATR than MCHS-OTR. Different $W_{con}/W_r$ leads to different attack angles of fluid flow to ribs and the different rib arrangement results in different converging-diverging-constant cross-section length ratio. Under those influences, the MCHS-ATR and MCHS-OTR show much different effect of rib's converging-diverging ratio on local fluid flow. Fig. 12c clearly demonstrates the movement of the $x$-location with the lowest $p_x$ and the variation of inverse pressure gradient when water flows across the triangular ribs with changed $W_{con}/W_r$. Corresponding to the variation of

$p_x$ with $W_{con}$, the MCHS-ATR shows much higher $f_xRe$ for $W_{con}/W_r$ = 0.1 as $W_r/W_c$ = 1 and obviously larger $f_xRe$ for $W_{con}/W_r$ = 0.1 and 0.9 as $W_r/W_c$ = 2, while the $f_xRe$ of MCHS-OTR does not change much with $W_{con}/W_r$.

Figures 14 and 15 show the effect of $W_{con}/W_r$ on $T_{w,x}$ and $Nu_x$ as $Re$ = 443. As $W_r/W_c$ = 1, the $W_{con}/W_r$ has less influence on $T_{w,x}$ for MCHS-ATR than MCHS-OTR, while as $W_r/W_c$ = 2, the $W_{con}/W_r$ shows obvious influence on $T_{w,x}$ for both MCHS-ATR and MCHS-OTR. As a consequence of variation of $T_{w,x}$ with $W_{con}/W_r$, the $Nu_x$ keeps around 11 for MCHS-ATR and changes in the range of 10.5 to 12.5 for MCHS-OTR as $W_r/W_c$ = 1, while the $Nu_x$ varies in the range of 8.5 to 13 for both MCHS-ATR and MCHS-OTR as $W_r/W_c$ = 2. As shown in Fig. 15, the MCHS-OTR with $W_{con}/W_r$ = 0.7 and 0.9 shows the highest $Nu_x$ at a specific $x^*$, where the channel with $W_{con}/W_r$ = 0.7 performs best as $W_r/W_c$ = 1 and the one with $W_{con}/W_r$ = 0.9 becomes optimal as $W_r/W_c$ = 2. And the MCHS-ATR with $W_{con}/W_r$ = 0.9 shows the best heat transfer performance as $W_r/W_c$ = 2.

*4.5. Effect of rib spacing on local fluid flow and heat transfer characteristics*

Figures 16 and 17 present the influence of $S_r$ on $p_x$ and $f_xRe$ as $Re$ = 443. The spacing of triangular ribs demonstrates an important influence on the local pressure characteristic that the $p_x$ at a specific position largely increases with the decrease of $S_r/W_c$ for both MCHS-ATR and MCHS-OTR. A lower $S_r/W_c$ means a shorter constant cross sectional area between triangular ribs, leading to a higher developing region effect and thus a larger pressure drop. It is also noted that a larger $S_r/W_c$ results in a larger pressure fluctuation as water flows cross the triangular ribs, especially for the MCHS-ATR. A larger $S_r/W_c$ brings about a more developed laminar flow upstream the triangular rib, and when it is interrupted, the fraction factor will changes much more. Particularly for the MCHS-ATR, the changed flow passage combined the interrupted boundary layer makes the local pressure fluctuate dramatically owing to the Bernoulli effect. As a result, the lower $S_r/W_c$ leads

to the larger fluctuation of $f_xRe$, especially for the MCHS-ATR. In addition, as shown in Fig. 17, for the cases with $S_r/W_c$ = 20 and 10, the $f_xRe$ with $x^+$ coincides with MCHS at the channel inlet due to the hydrodynamic developing region for both MCHS-ATR and MCHS-OTR, while for the cases with $S_r/W_c$ = 5 and 2.5, the $f_xRe$ with $x^+$ at the channel inlet is a little different from those with $S_r/W_c$ = 20 and 10 for both MCHS-ATR and MCHS-OTR, due to the short constant cross sectional area, where the triangular ribs has exerted an effect on the fluid flow characteristic.

Figures 18 and 19 illustrate the effect of rib spacing on local heat transfer characteristic as $Re$ = 443. As shown in Fig. 18, the $T_{w,x}$ at a given position largely decreases with the decrease of $S_r/W_c$. As discussed above, a lower $S_r/W_c$ results in a higher developing region in the constant cross sectional area and thus a better heat transfer performance. For $S_r/W_c$ = 20 and 10, the MCHS-ATR and MCHS-OTR show closed $T_{w,x}$ at a given position as $W_r$ = 0.1 mm, while the MCHS-ATR performs much better than MCHS-OTR as $W_r$ = 0.2 mm. For $S_r/W_c$ = 2.5, the MCHS-OTR shows a better heat transfer performance than MCHS-ATR as both $W_r$ = 0.1 and 0.2 mm. Along the whole length of microchannel, the $T_{w,x}$ is increased by 13.3, 11.7, 10.4 and 9.5 K as $W_r$ = 0.1 mm and 15.4, 13.4, 11.6 and 10.1 K as $W_r$ = 0.2 mm respectively for MCHS-ATR with $S_r/W_c$ = 20, 10, 5 and 2.5, and 14.3, 11.4, 10.2 and 9.1 K as $W_r$ = 0.1 mm and 19.8, 18.5, 10.0 and 9.7 K as $W_r$ = 0.2 mm respectively for MCHS-OTR with $S_r/W_c$ = 20, 10, 5 and 2.5. Consequently, the $Nu_x$ at a specific position obviously increases with decrease of $S_r/W_c$ and a lower $S_r/W_c$ results in a higher $Nu_x$ with no obvious drop along the flow direction. The MCHS-OTR with $S_r/W_c$ = 2.5 presents the highest average Nusselt number, which is 13.1 as $W_r$ = 0.1 mm and 12.1 as $W_r$ = 0.2 mm, respectively 2.15 and 1.98 times higher than the reference MCHS. It is also noticed that as $W_r/W_c$ = 2, the MCHS-ATR shows much higher $Nu_x$ a specific $x^*$ than MCHS-OTR for $S_r/W_c$ = 20 and 10, while the MCHS-OTR performs much better for $S_r/W_c$ = 2.5.

## 5. Conclusions

The heat transfer mechanism of laminar flow in microchannel heat sinks with triangular ribs on sidewalls was studied numerically and the effects of triangular ribs' geometry and arrangement on local fluid flow and heat transfer characteristics are investigated extensively. Based on the numerical results, the following conclusions can be drawn:

(1) Triangular ribs mounted on the parallel sidewalls of microchannels can significantly reduce the temperature rise of the heat sink base and efficiently prevent the drop of local heat transfer coefficient along the flow direction, but also result in higher local friction factor than the straight microchannel. These characteristics are caused by the repeated redeveloping of boundary layer, the enhanced convective fluid mixing, the increased heat transfer surface area, and the recirculation formed downstream of triangular ribs. The first three mechanisms lead to heat transfer enhancement but larger pressure drop, and the fourth improve or deteriorate heat transfer, dependent on the intensity and regime of the developed second flow.

(2) Aligned and offset arrangement of triangular ribs result in much different local fluid flow and heat transfer characteristics. Local pressure and heat transfer coefficient fluctuate from one triangular rib to the next and their amplitude and wavelength significantly depend on the geometry and arrangement of triangular ribs. The MCHS-ATR exerts an influence on the local thermohydraulic performance mainly through the changed flow passage as the converging–diverging channel, leading to much large fluctuation of local pressure and heat transfer. The MCHS-OTR affects the local laminar flow and heat transfer mostly by the altered flow direction as the wavy channel, and partly by the changed flow passage, which can result in similar heat transfer performance but much smaller pressure drop and lead to much smaller fluctuation of local pressure and heat transfer than the

MCHS-ATR.

(3) Geometry of triangular ribs shows significant influence on local thermohydraulic performance. With the increasing of rib width, the local pressure and local heat transfer at a specific position first decreases and then increases. A lower rib height cannot exert obvious influence on local thermohydraulic performance, while the larger one can lead to significant increase of local pressure and local heat transfer. The rib's converging-diverging ratio combines the rib width to affect the local pressure and heat transfer. A smaller rib spacing lead to dramatic increase of local pressure drop and local heat transfer.

(4) For the studied geometry of triangular ribs and Reynolds number, with increase of $H_r$ from 0.005 to 0.025 mm, the $T_{w,x}$ increase of MCHS-ATR along the whole channel length declines from 18.9 to 10.0 K as $W_r$ = 0.1 mm and from 19.9 to 9.9 K as $W_r$ = 0.2 mm, and that of MCHS-OTR drops from 19.1 to 9.9 K as $W_r$ = 0.1 mm and from 19.8 to 9.8 K as $W_r$ = 0.2 mm; With decrease of $S_r$ from 2 to 0.25 mm, the $T_{w,x}$ increase of MCHS-ATR along the whole channel length decreases from 13.3 to 9.5 K as $W_r$ = 0.1 mm and from 15.4 to 10.1 K as $W_r$ = 0.2 mm, and that of MCHS-OTR declines from 14.3 to 9.1 K as $W_r$ = 0.1 mm and from 19.8 to 9.7 K as $W_r$ = 0.2 mm. Compared to the reference straight microchannel heat sink, a superior configuration (MCHS-OTR with $W_r$ = 0.1 mm, $H_r$ = 0.025 mm, $W_{con}$ = 0.07 mm and $S_r$ = 0.25 mm) can yield an improvement of up to 2.15 times higher of average Nusselt number.

**Acknowledgements**

The work was supported by the Engineering and Physical Sciences Research Council (EPSRC) of the UK through research grant (RRR1025R33470) and the Youth Innovation Promotion Association of CAS (2016131).

**References**


[1] D.B. Tuckerman, R.F.W. Pease, High-performance heat sinking for VLSI, IEEE Electron Device Letters 2 (1981) 126–129.

[2] L. Chai, G.D. Xia, J.Z. Qi, Experimental and numerical study of flow and heat transfer in trapezoidal microchannels, Heat Transfer Engineering 33 (2012) 972–981.

[3] S.G. Kandlikar, S. Colin, Y. Peles, S. Garimella, R.F. Pease, J.J. Brandner, D.B. Tuckerman, Heat transfer in microchannels—2012 status and research needs, Journal of Heat Transfer 135 (2013) 091001.

[4] N.A.C. Sidik, M.N.A.W. Muhamad, W.M.A.A, An overview of passive techniques for heat transfer augmentation in microchannel heat sink, International Communications in Heat and Mass Transfer 88 (2017) 74–83.

[5] J.L. Xu, Y.H. Gan, D.C. Zhang, Microscale heat transfer enhancement using thermal boundary layer redeveloping concept, International Journal of Heat and Mass Transfer 48 (2005) 1662–1674.

[6] J.L Xu, Y.X Song, W. Zhang, Numerical simulations of interrupted and conventional microchannel heat sinks, International Journal of Heat and Mass Transfer 51 (2008) 5906–5917.

[7] L. Chai, G.D. Xia, M. Zhou, J. Li, J. Qi, Optimum thermal design of interrupted microchannel heat sink with rectangular ribs in the transverse microchambers, Applied Thermal Engineering 51 (2013) 880–889.

[8] L. Chai, G.D. Xia, H.S. Wang, Laminar flow and heat transfer characteristics of interrupted microchannel heat sink with ribs in the transverse microchambers, International Journal of Thermal Sciences 110 (2016) 1–11.

[9] L. Chai, L. Wang, Thermohydraulic performance of interrupted microchannel heat sinks with different

rib geometries in transverse microchambers, International Journal of Thermal Sciences 127 (2018) 201–212.

[10] K.C. Wong, J.H. Lee, Investigation of thermal performance of microchannel heat sink with triangular ribs in the transverse microchambers, International Communications in Heat and Mass Transfer 65 (2015) 103–110.

[11] P. Promvonge, S. Sripattanapipat, S. Kwankaomeng, Laminar periodic flow and heat transfer in square channel with 45º inline baffles on two opposite walls, International Journal of Thermal Sciences 49 (2010) 963–975.

[12] C. Liu, J. Teng, J.C. Chu, Experimental investigations on liquid flow and heat transfer in rectangular microchannel with longitudinal vortex generators, International Journal of Heat and Mass Transfer 54 (2011) 3069–3080.

[13] A. Ebrahimi, R. Ehsan Roohi, K. Saeid, Numerical study of liquid flow and heat transfer in rectangular microchannel with longitudinal vortex generators, Applied Thermal Engineering 78 (2015) 576–583.

[14] A.J. Foong, N. Ramesh, T.T. Chandratilleke, Laminar convective heat transfer in a microchannel with internal longitudinal fins, International Journal of Thermal Sciences 48 (2009) 1908–1913.

[15] G. Xie, H Shen, C.C. Wang, Parametric study on thermal performance of microchannel heat sinks with internal vertical Y-shaped bifurcations, International Journal of Heat and Mass Transfer 90 (2015) 948–958.

[16] Y. Sui, C.J. Teo, P.S. Lee, Fluid flow and heat transfer in wavy microchannels, International Journal of Heat and Mass Transfer 53 (2010) 2760–2772.

[17] Y. Sui, P.S. Lee, C.J. Teo, An experimental study of flow friction and heat transfer in wavy microchannels with rectangular cross section, International Journal of Thermal Sciences 50 (2011)

2473–2482.

[18] H.A. Mohammed, P. Gunnasegaran, N.H. Shuaib, Numerical simulation of heat transfer enhancement in wavy microchannel heat sink, International Communications in Heat and Mass Transfer 38 (2011) 63–68.

[19] L. Lin, J. Zhao, G Lu, X.D. Wang, W.M. Yan, Heat transfer enhancement in microchannel heat sink by wavy channel with changing wavelength/amplitude, International Journal of Thermal Sciences 118 (2017) 423–434.

[20] H. Ghaedamini, P.S. Lee, C.J. Teo, Developing forced convection in converging–diverging microchannels, International Journal of Heat and Mass Transfer 65 (2013) 491-499.

[21] L. Chai, G.D. Xia, M.Z. Zhou, Numerical simulation of fluid flow and heat transfer in a microchannel heat sink with offset fan-shaped reentrant cavities in sidewall, International Communications in Heat and Mass Transfer 38 (2011) 577–584.

[22] L. Chai, G.D. Xia, L. Wang, M.Z. Zhou, Z.Z. Cui, Heat transfer enhancement in microchannel heat sinks with periodic expansion–constriction cross-sections, International Journal of Heat and Mass Transfer 62 (2013) 741–751.

[23] G.D. Xia, L. Chai, M.Z. Zhou, Effects of structural parameters on fluid flow and heat transfer in a microchannel with aligned fan-shaped reentrant cavities, International Journal of Thermal Sciences 50 (2011) 411–419.

[24] G.D. Xia, L. Chai, H.Y. Wang, Optimum thermal design of microchannel heat sink with triangular reentrant cavities, Applied Thermal Engineering 31 (2011) 1208–1219.

[25] L. Chai, G.D. Xia, H.S. Wang, Numerical study of laminar flow and heat transfer in microchannel heat sink with offset ribs on sidewalls, Applied Thermal Engineering 92 (2016) 32–41

[26] L. Chai, G.D. Xia, H.S. Wang, Parametric study on thermal and hydraulic characteristics of laminar flow in microchannel heat sink with fan-shaped ribs on sidewalls–Part 1: Heat transfer, International Journal of Heat and Mass Transfer 97 (2016) 1069–1080.

[27] L. Chai, G.D. Xia, H.S. Wang, Parametric study on thermal and hydraulic characteristics of laminar flow in microchannel heat sink with fan-shaped ribs on sidewalls–Part 2: Pressure drop, International Journal of Heat and Mass Transfer 97 (2016) 1081–1090.

[28] L. Chai, G.D. Xia, H.S. Wang, Parametric study on thermal and hydraulic characteristics of laminar flow in microchannel heat sink with fan-shaped ribs on sidewalls–Part 3: Performance evaluation, International Journal of Heat and Mass Transfer 97 (2016) 1091–1101

[29] G.D. Xia, Y.L. Zhai, Z.Z. Cui, Numerical investigation of thermal enhancement in a micro heat sink with fan-shaped reentrant cavities and internal ribs, Applied Thermal Engineering 58 (2013) 52–60.

[30] Y.L. Zhai, G.D. Xia, X.F. Liu, Heat transfer in the microchannels with fan-shaped reentrant cavities and different ribs based on field synergy principle and entropy generation analysis, International journal of heat and mass transfer 68 (2014) 224–233.

[31] Y.F. Li, G.D. Xia, D.D. Ma, Characteristics of laminar flow and heat transfer in microchannel heat sink with triangular cavities and rectangular ribs, International Journal of Heat and Mass Transfer 98 (2016) 17–28.

[32] I.A. Ghani, N. Kamaruzaman, N.A.C. Sidik, Heat transfer augmentation in a microchannel heat sink with sinusoidal cavities and rectangular ribs, International Journal of Heat and Mass Transfer 108 (2017) 1969–1981.

[33] F. Incropera, Liquid Cooling of Electronic Devices by Single-Phase Convection, Wiley, 1999.

**Nomenclature**

| | |
|---|---|
| $A$ | area, $m^2$ |
| $c_p$ | specific heat, $J \cdot kg^{-1} K^{-1}$ |
| $D_h$ | hydraulic diameter, m |
| $f$ | friction factor |
| $\overline{f}$ | average friction factor |
| $h$ | heat transfer coefficient, $W \cdot m^{-2} K^{-1}$ |
| $\overline{h}$ | average heat transfer coefficient, $W \cdot m^{-2} K^{-1}$ |
| $H$ | height, m |
| $k$ | thermal conductivity, $W \cdot m^{-1} \cdot K^{-1}$ |
| $L$ | length, m |
| $Nu$ | Nusselt number |
| $\overline{Nu}$ | average Nusselt number |
| $p$ | pressure, Pa |
| $q$ | heat flux, $W \cdot m^{-2}$ |
| $Re$ | Reynolds number |
| $S$ | spacing, m |
| $T$ | temperature, K |
| $\overline{T}$ | average temperature, K |
| $u$ | velocity, $m \cdot s^{-1}$ |
| $\overline{u}$ | average velocity, $m \cdot s^{-1}$ |
| $W$ | width, m |

| | |
|---|---|
| $x^+$ | non-dimensionalized length, $x^+ = x/(D_h Re)$ |
| $x^*$ | non-dimensionalized length, $x^* = x/(D_h RePr)$ |
| $x,y,z$ | three coordinates shown in Fig. 1a, m |
| Greek letters | |
| $\rho$ | density, $kg \cdot m^{-3}$ |
| $\mu$ | dynamic viscosity, Pa·s |
| *Subscripts* | |
| c | channel |
| com | computational domain |
| con | contraction |
| exp | experimental |
| f | fluid |
| in | inlet |
| out | outlet |
| r | rib |
| s | silicon |
| $x$ | flow direction |
| w | heat sink base |
| *Abbreviations* | |
| ATR | aligned triangular ribs |
| CFD | computational fluid dynamics |
| LVG | longitudinal vortex generators |

| | |
|---|---|
| MCHS | microchannel heat sink |
| OTR | offset triangular ribs |

**Figure captions**

Table 1 Temperature-dependent property equations of water [33].

Table 2 Boundary conditions.

Table 3 Geometry parameters of triangular rib in CFD plots.

Fig. 1 Microchannel heat sinks with triangular ribs on sidewalls. (a) Computational domain. (b) Geometry parameters and arrangement of triangular ribs.

Fig. 2 Verification of numerical model.

Fig. 3 Velocity contour.

Fig. 4 Pressure distribution.

Fig. 5 Temperature field.

Fig. 6 Effects of rib width on local hydraulic characteristics. (a) $p_x$ versus $x$. (b) variation of $p_x$ for 5.6 mm < $x$ < 7.2 mm. (c) $f_xRe$ versus $x^+$.

Fig. 7 Effects of rib width on local heat transfer characteristics. (a) $T_{w,x}$ versus $x$. (b) $Nu_x$ versus $x^*$.

Fig. 8 $p_x$ versus $x$ for different $H_r/W_c$. (a) as $W_r/W_c$ = 1, $W_{con}/W_r$ = 0.7 and $S_r/W_c$ = 4. (b) as $W_r/W_c$ = 2, $W_{con}/W_r$ = 0.7 and $S_r/W_c$ = 4. (c) as 6 mm < $x$ < 6.8 mm.

Fig. 9 $f_xRe$ versus $x^+$ for different $H_r/W_c$. (a) as $W_r/W_c$ = 1, $W_{con}/W_r$ = 0.7 and $S_r/W_c$ = 4. (b) as $W_r/W_c$ = 2, $W_{con}/W_r$ = 0.7 and $S_r/W_c$ = 4.

Fig. 10 $T_{w,x}$ versus $x$ for different $H_r/W_c$. (a) as $W_r/W_c$ = 1, $W_{con}/W_r$ = 0.7 and $S_r/W_c$ = 4. (b) as $W_r/W_c$ = 2, $W_{con}/W_r$ = 0.7 and $S_r/W_c$ = 4.

Fig. 11 $Nu_x$ versus $x^*$ for different $H_r/W_c$. (a) as $W_r/W_c$ = 1, $W_{con}/W_r$ = 0.7 and $S_r/W_c$ = 4. (b) as $W_r/W_c$ = 2, $W_{con}/W_r$ = 0.7 and $S_r/W_c$ = 4.

Fig. 12 $p_x$ versus $x$ for different $W_{con}/W_r$. (a) as $W_r/W_c$ = 1, $H_r/W_c$ =0.25 and $S_r/W_c$ = 4. (b) as $W_r/W_c$ = 2, $H_r/W_c$ =0.25 and $S_r/W_c$ = 4. (c) as 6 mm < $x$ < 6.8 mm.

Fig. 13 $f_xRe$ versus $x^+$ for different $W_{con}/W_r$. (a) as $W_r/W_c$ = 1, $H_r/W_c$ =0.25 and $S_r/W_c$ = 4. (b) as $W_r/W_c$ = 2, $H_r/W_c$ =0.25 and $S_r/W_c$ = 4.

Fig. 14 $T_{w,x}$ versus $x$ for different $W_{con}/W_r$. (a) as $W_r/W_c$ = 1, $H_r/W_c$ =0.25 and $S_r/W_c$ = 4. (b) as $W_r/W_c$ = 2, $H_r/W_c$ =0.25 and $S_r/W_c$ = 4.

Fig. 15 $Nu_x$ versus $x^*$ for different $W_{con}/W_r$. (a) as $W_r/W_c$ = 1, $H_r/W_c$ =0.25 and $S_r/W_c$ = 4. (b) as $W_r/W_c$ = 2, $H_r/W_c$ =0.25 and $S_r/W_c$ = 4.

Fig. 16 $p_x$ versus $x$ for different $S_r/W_c$. (a) as $W_r/W_c$ = 1, $H_r/W_c$ =0.25 and $W_{con}/W_r$ = 0.7. (b) as $W_r/W_c$ = 2, $H_r/W_c$ =0.25 and $W_{con}/W_r$ = 0.7.

Fig. 17 $f_xRe$ versus $x^+$ for different $S_r/W_c$. (a) as $W_r/W_c$ = 1, $H_r/W_c$ =0.25 and $W_{con}/W_r$ = 0.7. (b) as $W_r/W_c$ = 2, $H_r/W_c$ =0.25 and $W_{con}/W_r$ = 0.7.

Fig. 18 $T_{w,x}$ versus $x$ for different $S_r/W_c$. (a) as $W_r/W_c$ = 1, $H_r/W_c$ =0.25 and $W_{con}/W_r$ = 0.7. (b) as $W_r/W_c$ = 2, $H_r/W_c$ =0.25 and $W_{con}/W_r$ = 0.7.

Fig. 19 $Nu_x$ versus $x^*$ for different $S_r/W_c$. (a) as $W_r/W_c$ = 1, $H_r/W_c$ =0.25 and $W_{con}/W_r$ = 0.7. (b) as $W_r/W_c$ = 2, $H_r/W_c$ =0.25 and $W_{con}/W_r$ = 0.7.

Table 1 Temperature-dependent property equations of water [33].

$$\rho_{\mathrm{f}} = \frac{999.84 + 18.225T - 7.92\times10^{-3}T^2 - 5.545\times10^{-5}T^3 + 1.498\times10^{-7}T^4 - 3.933\times10^{-10}T^5}{1 + 1.816\times10^{-2}T} \tag{5}$$

$$\mu_{\mathrm{f}} = 2.414\times10^{-5}\times10^{\frac{247.8}{T-140}} \tag{6}$$

$$c_{\mathrm{pf}} = 8958.9 - 40.535T + 0.11243T^2 - 1.014\times10^{-4}T^3 \tag{7}$$

$$k_{\mathrm{f}} = -0.58166 + 6.3556\times10^{-3}T - 7.964\times10^{-6}T^2 \tag{8}$$

where the unit of $T$ is $^{\mathrm{o}}$C in Eq. (5) and K in Eqs. (6), (7) and (8).

Table 2 Boundary conditions.

| | | |
|---|---|---|
| Velocity-inlet boundary | $x = 0$: $u = u_{in}$ and $T_f = T_{in}$ | (9) |
| Pressure-outlet boundary | $x = 10$ mm: $p_f = p_{out}$ | (10) |
| Constant heat flux boundary | $z = 0$: $-k_s \frac{\partial T_s}{\partial z} = q_w$ | (11) |
| Symmetry wall boundary | $y = 0$ and $y = 0.25$ mm, $\frac{\partial T_s}{\partial y} = 0$ | (12) |
| Adiabatic boundary | All other surfaces, $\frac{\partial T_f}{\partial x} = 0$ or $\frac{\partial T_s}{\partial x} = 0$ | (13) |

Table 3 Geometry parameters of triangular rib in CFD plots.

| Heat sink | Rib arrangement | $W_r$ (mm) | $H_r$ (mm) | $W_{con}$ (mm) | $S_r$ (mm) |
|---|---|---|---|---|---|
| MCHS-ATR1 | aligned | 0.1 | 0.025 | 0.07 | 0.4 |
| MCHS-OTR1 | offset | 0.1 | 0.025 | 0.07 | 0.4 |
| MCHS-ATR2 | aligned | 0.2 | 0.025 | 0.07 | 0.4 |
| MCHS-OTR2 | offset | 0.2 | 0.025 | 0.07 | 0.4 |

Fig. 1

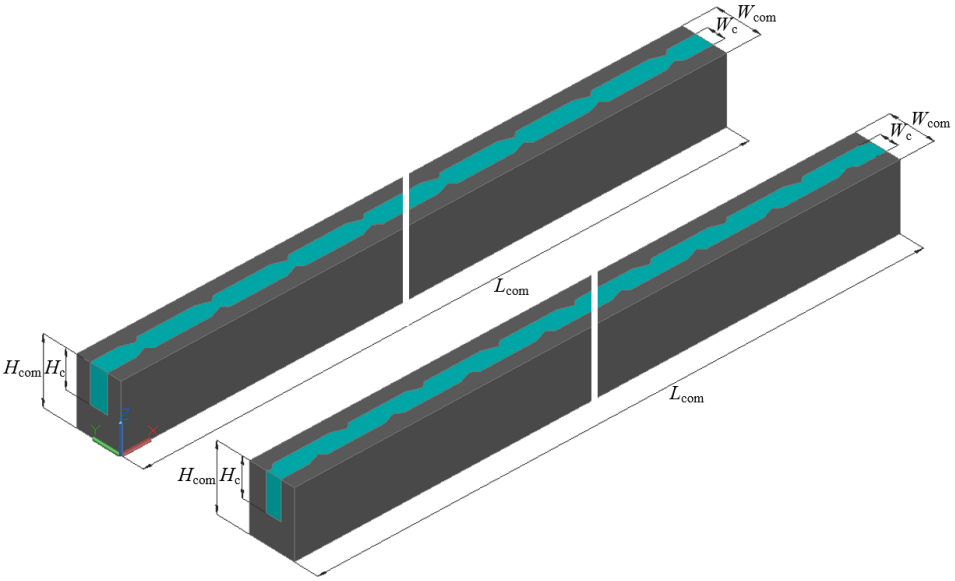
$W_{com}$
$W_c$
$L_{com}$
$H_{com}$
$H_c$

(a)

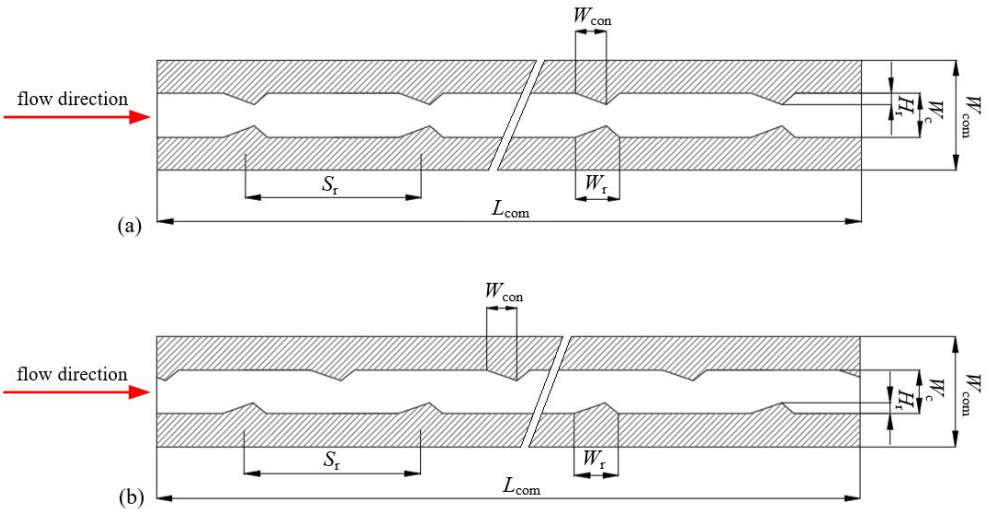
flow direction
$W_{con}$
$H_r$
$W_c$
$W_{com}$
$S_r$
$W_r$
$L_{com}$
(a)
flow direction
$W_{con}$
$H_r$
$W_c$
$W_{com}$
$S_r$
$W_r$
$L_{com}$
(b)

(b)

Fig. 2

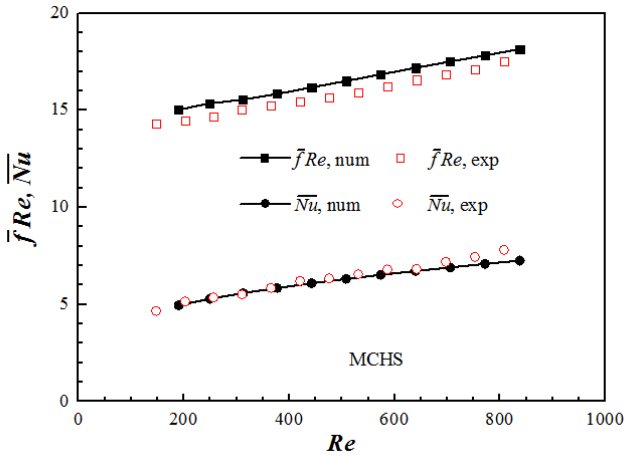
20
15
10
5
0
0
200
400
600
800
1000
Re
$\bar{f}Re$, $\overline{Nu}$
$\bar{f}Re$, num
$\bar{f}Re$, exp
$\overline{Nu}$, num
$\overline{Nu}$, exp
MCHS

Fig. 3

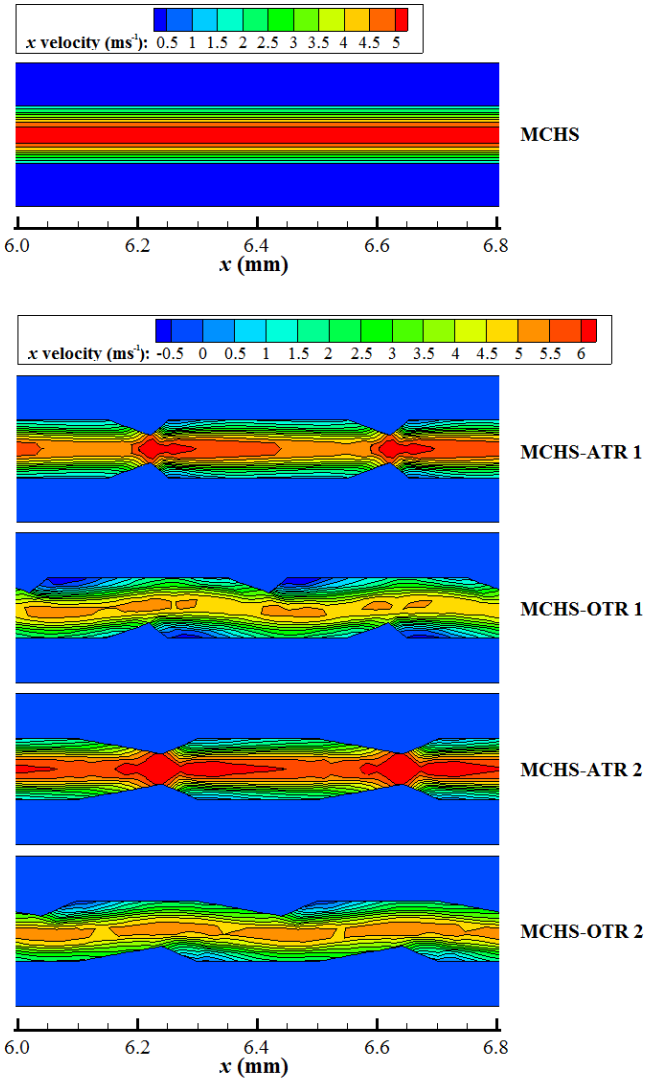
x velocity (ms-1): 0.5 1 1.5 2 2.5 3 3.5 4 4.5 5
MCHS
6.0
6.2
6.4
6.6
6.8
x (mm)
x velocity (ms-1): -0.5 0 0.5 1 1.5 2 2.5 3 3.5 4 4.5 5 5.5 6
MCHS-ATR 1
MCHS-OTR 1
MCHS-ATR 2
MCHS-OTR 2
6.0
6.2
6.4
6.6
6.8
x (mm)

Fig. 4

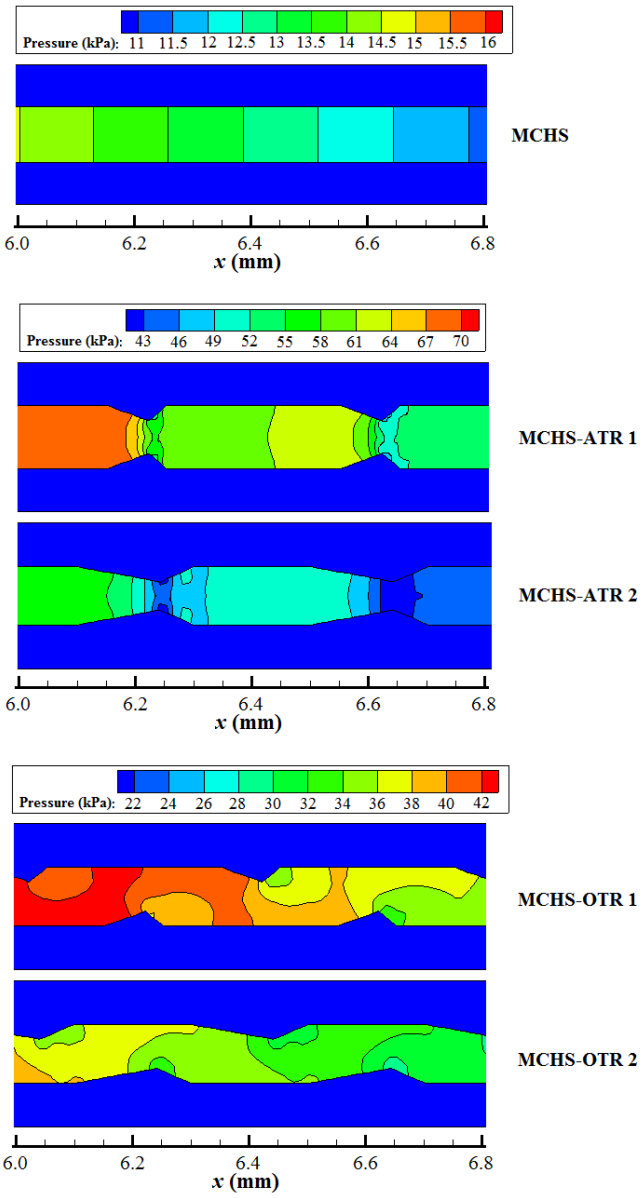
Pressure (kPa): 11 11.5 12 12.5 13 13.5 14 14.5 15 15.5 16
MCHS
6.0 6.2 6.4 6.6 6.8
x (mm)
Pressure (kPa): 43 46 49 52 55 58 61 64 67 70
MCHS-ATR 1
MCHS-ATR 2
6.0 6.2 6.4 6.6 6.8
x (mm)
Pressure (kPa): 22 24 26 28 30 32 34 36 38 40 42
MCHS-OTR 1
MCHS-OTR 2
6.0 6.2 6.4 6.6 6.8
x (mm)

Fig. 5

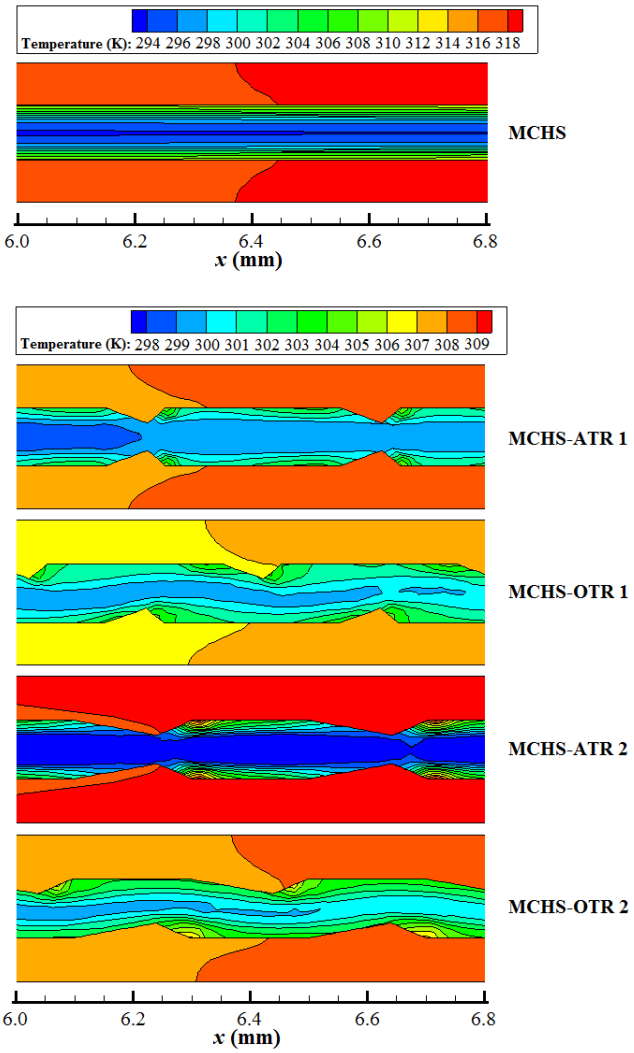
Temperature (K): 294 296 298 300 302 304 306 308 310 312 314 316 318
MCHS
6.0
6.2
6.4
6.6
6.8
x (mm)
Temperature (K): 298 299 300 301 302 303 304 305 306 307 308 309
MCHS-ATR 1
MCHS-OTR 1
MCHS-ATR 2
MCHS-OTR 2
6.0
6.2
6.4
6.6
6.8
x (mm)

Fig. 6

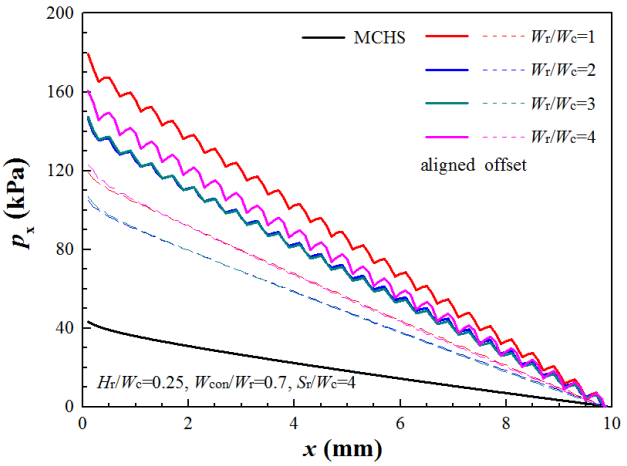
MCHS
$W_f/W_c$=1
$W_f/W_c$=2
$W_f/W_c$=3
$W_f/W_c$=4
aligned offset
$H_f/W_c$=0.25, $W_{con}/W_f$=0.7, $S_f/W_c$=4
$p_x$ (kPa)
$x$ (mm)

(a)

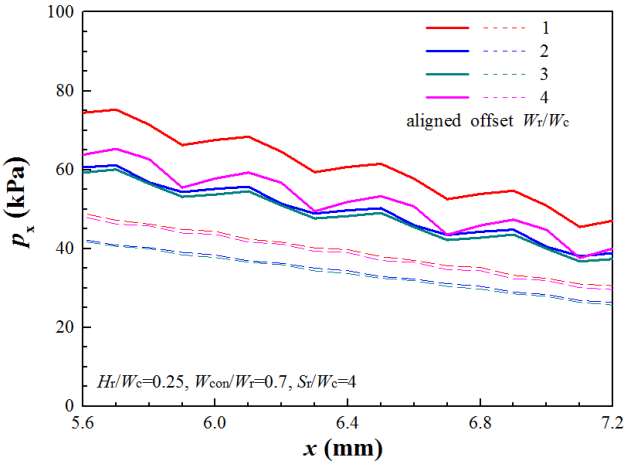
1
2
3
4
aligned offset $W_f/W_c$
$H_f/W_c$=0.25, $W_{con}/W_f$=0.7, $S_f/W_c$=4
$p_x$ (kPa)
$x$ (mm)

(b)

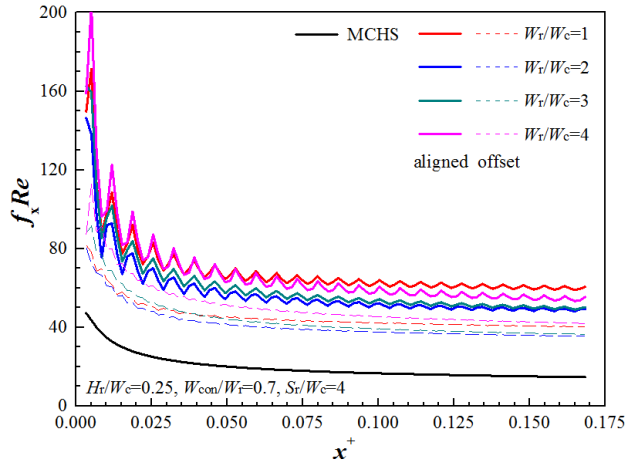
MCHS
$W_f/W_c$=1
$W_f/W_c$=2
$W_f/W_c$=3
$W_f/W_c$=4
aligned offset
$H_f/W_c$=0.25, $W_{con}/W_f$=0.7, $S_f/W_c$=4
$f_x Re$
$x^+$

(c)

Fig. 7

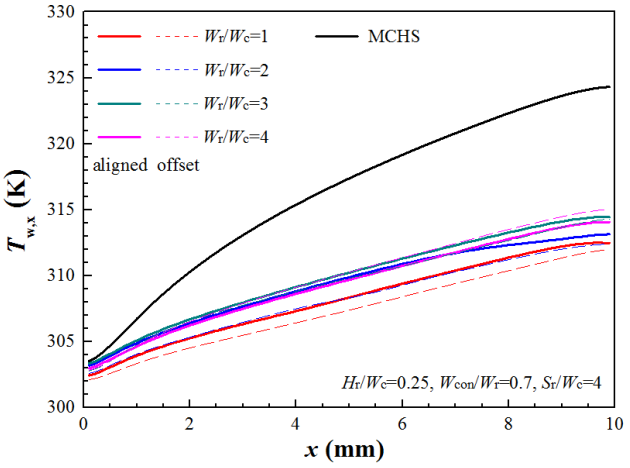
330
325
320
315
310
305
300
0
2
4
6
8
10
$T_{w,x}$ (K)
x (mm)
$W_r/W_c$=1
$W_r/W_c$=2
$W_r/W_c$=3
$W_r/W_c$=4
MCHS
aligned offset
$H_r/W_c$=0.25, $W_{con}/W_r$=0.7, $S_r/W_c$=4

(a)

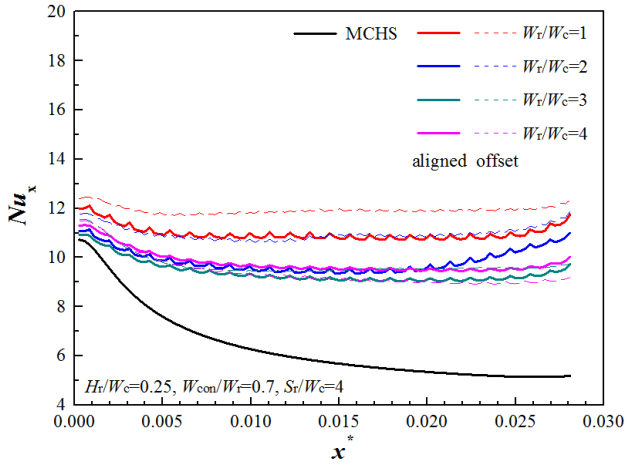
20
18
16
14
12
10
8
6
4
0.000
0.005
0.010
0.015
0.020
0.025
0.030
$Nu_x$
$x^*$
MCHS
$W_r/W_c$=1
$W_r/W_c$=2
$W_r/W_c$=3
$W_r/W_c$=4
aligned offset
$H_r/W_c$=0.25, $W_{con}/W_r$=0.7, $S_r/W_c$=4

(b)

Fig. 8

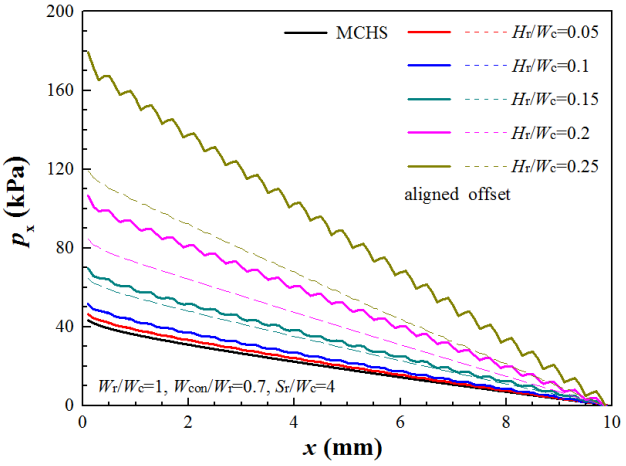
MCHS
$H_f/W_c$=0.05
$H_f/W_c$=0.1
$H_f/W_c$=0.15
$H_f/W_c$=0.2
$H_f/W_c$=0.25
aligned offset
$W_f/W_c$=1, $W_{con}/W_f$=0.7, $S_f/W_c$=4
$p_x$ (kPa)
$x$ (mm)

(a)

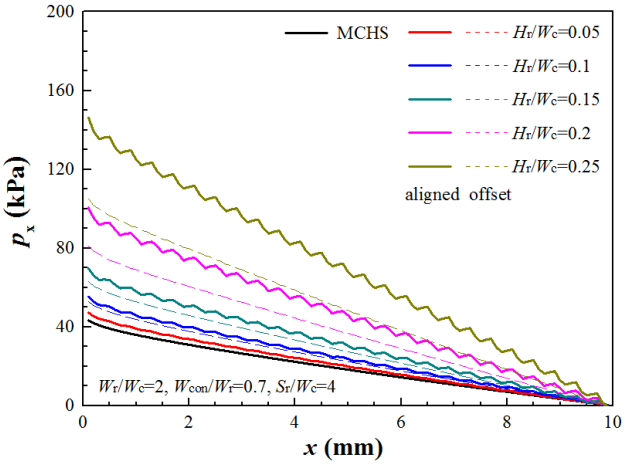
MCHS
$H_f/W_c$=0.05
$H_f/W_c$=0.1
$H_f/W_c$=0.15
$H_f/W_c$=0.2
$H_f/W_c$=0.25
aligned offset
$W_f/W_c$=2, $W_{con}/W_f$=0.7, $S_f/W_c$=4
$p_x$ (kPa)
$x$ (mm)

(b)

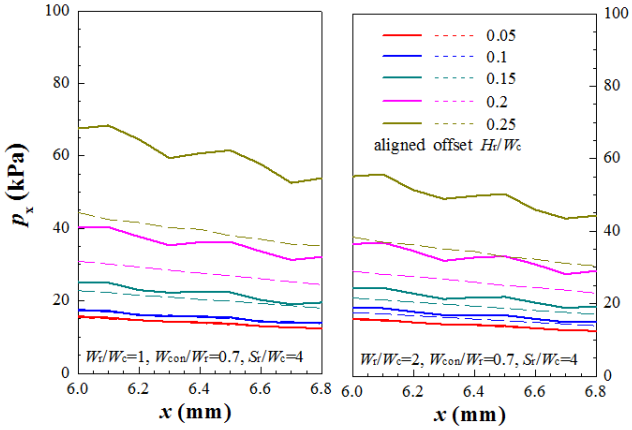
0.05
0.1
0.15
0.2
0.25
aligned offset $H_f/W_c$
$W_f/W_c$=1, $W_{con}/W_f$=0.7, $S_f/W_c$=4
$W_f/W_c$=2, $W_{con}/W_f$=0.7, $S_f/W_c$=4
$p_x$ (kPa)
$x$ (mm)

(c)

Fig. 9

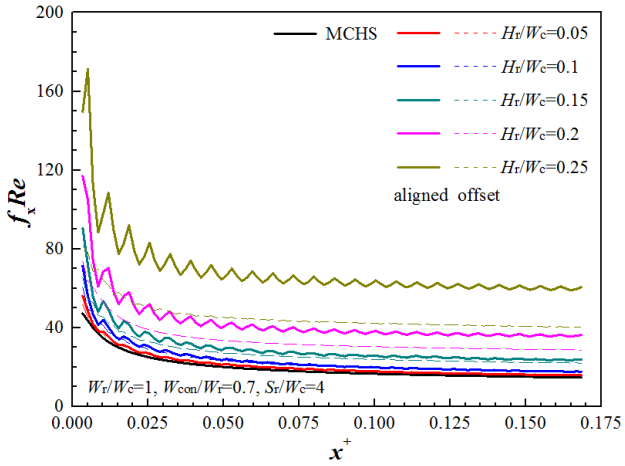
MCHS
$H_r/W_c$=0.05
$H_r/W_c$=0.1
$H_r/W_c$=0.15
$H_r/W_c$=0.2
$H_r/W_c$=0.25
aligned offset
$W_r/W_c$=1, $W_{con}/W_r$=0.7, $S_r/W_c$=4
$f_x Re$
$x^+$
0
40
80
120
160
200
0.000
0.025
0.050
0.075
0.100
0.125
0.150
0.175

(a)

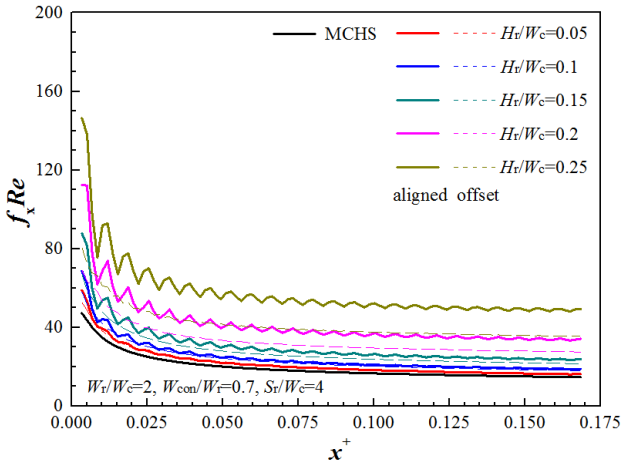
MCHS
$H_r/W_c$=0.05
$H_r/W_c$=0.1
$H_r/W_c$=0.15
$H_r/W_c$=0.2
$H_r/W_c$=0.25
aligned offset
$W_r/W_c$=2, $W_{con}/W_r$=0.7, $S_r/W_c$=4
$f_x Re$
$x^+$
0
40
80
120
160
200
0.000
0.025
0.050
0.075
0.100
0.125
0.150
0.175

(b)

Fig. 10

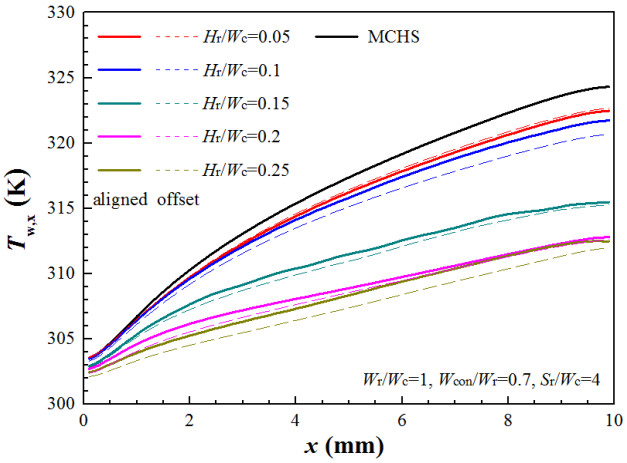
$H_r/W_c$=0.05
$H_r/W_c$=0.1
$H_r/W_c$=0.15
$H_r/W_c$=0.2
$H_r/W_c$=0.25
MCHS
aligned offset
$W_r/W_c$=1, $W_{con}/W_r$=0.7, $S_r/W_c$=4
$T_{w,x}$ (K)
$x$ (mm)
330
325
320
315
310
305
300
0
2
4
6
8
10

(a)

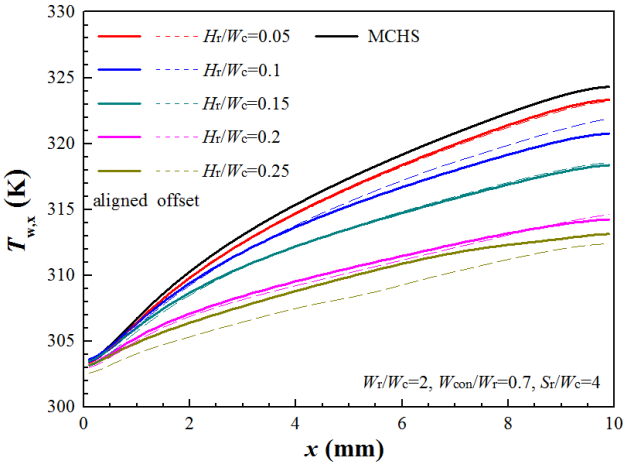
$H_r/W_c$=0.05
$H_r/W_c$=0.1
$H_r/W_c$=0.15
$H_r/W_c$=0.2
$H_r/W_c$=0.25
MCHS
aligned offset
$W_r/W_c$=2, $W_{con}/W_r$=0.7, $S_r/W_c$=4
$T_{w,x}$ (K)
$x$ (mm)
330
325
320
315
310
305
300
0
2
4
6
8
10

(b)

Fig. 11

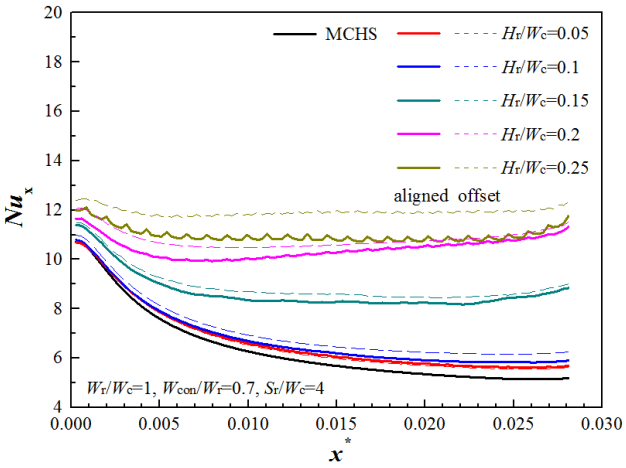
MCHS
$H_T/W_c$=0.05
$H_T/W_c$=0.1
$H_T/W_c$=0.15
$H_T/W_c$=0.2
$H_T/W_c$=0.25
aligned offset
$W_T/W_c$=1, $W_{con}/W_f$=0.7, $S_T/W_c$=4
$Nu_x$
$x^*$

(a)

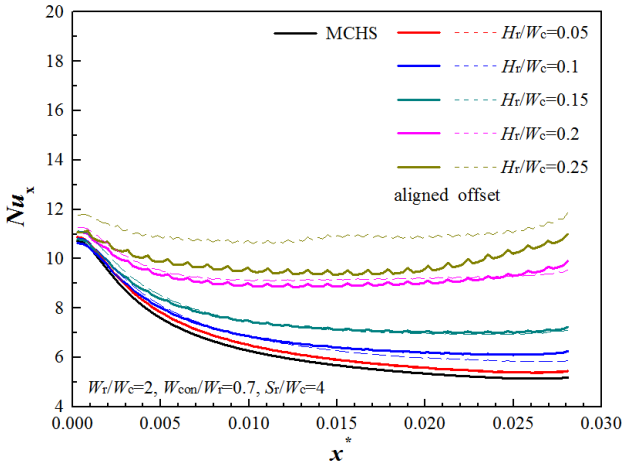
MCHS
$H_T/W_c$=0.05
$H_T/W_c$=0.1
$H_T/W_c$=0.15
$H_T/W_c$=0.2
$H_T/W_c$=0.25
aligned offset
$W_T/W_c$=2, $W_{con}/W_f$=0.7, $S_T/W_c$=4
$Nu_x$
$x^*$

(b)

Fig. 12

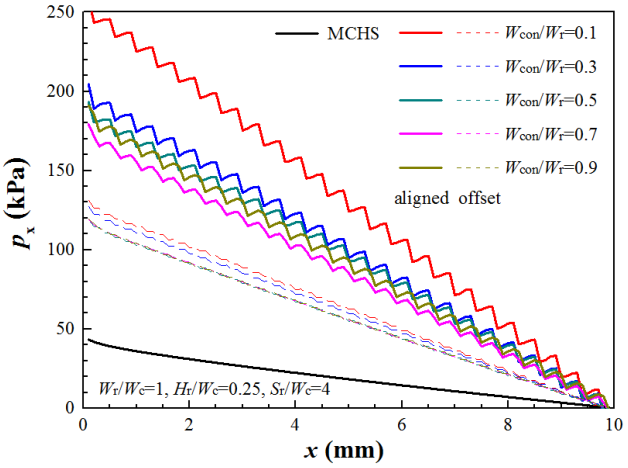
MCHS
$W_{con}/W_t$=0.1
$W_{con}/W_t$=0.3
$W_{con}/W_t$=0.5
$W_{con}/W_t$=0.7
$W_{con}/W_t$=0.9
aligned offset
$W_t/W_c$=1, $H_t/W_c$=0.25, $S_t/W_c$=4
$p_x$ (kPa)
$x$ (mm)

(a)

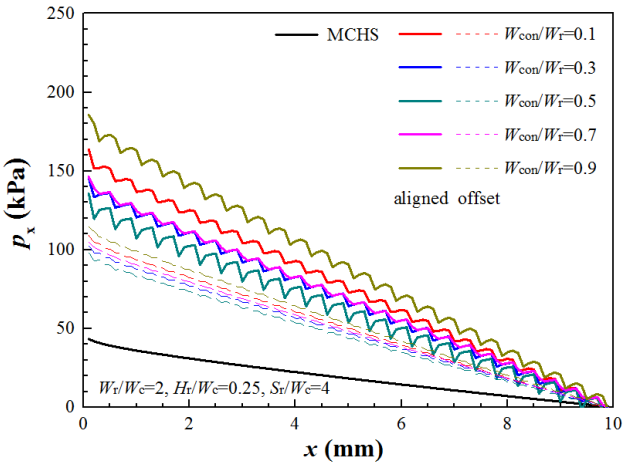
MCHS
$W_{con}/W_t$=0.1
$W_{con}/W_t$=0.3
$W_{con}/W_t$=0.5
$W_{con}/W_t$=0.7
$W_{con}/W_t$=0.9
aligned offset
$W_t/W_c$=2, $H_t/W_c$=0.25, $S_t/W_c$=4
$p_x$ (kPa)
$x$ (mm)

(b)

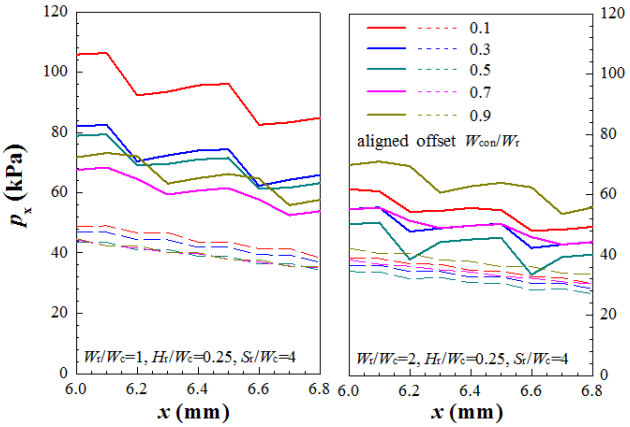
0.1
0.3
0.5
0.7
0.9
aligned offset $W_{con}/W_t$
$W_t/W_c$=1, $H_t/W_c$=0.25, $S_t/W_c$=4
$W_t/W_c$=2, $H_t/W_c$=0.25, $S_t/W_c$=4
$p_x$ (kPa)
$x$ (mm)

(c)

Fig. 13

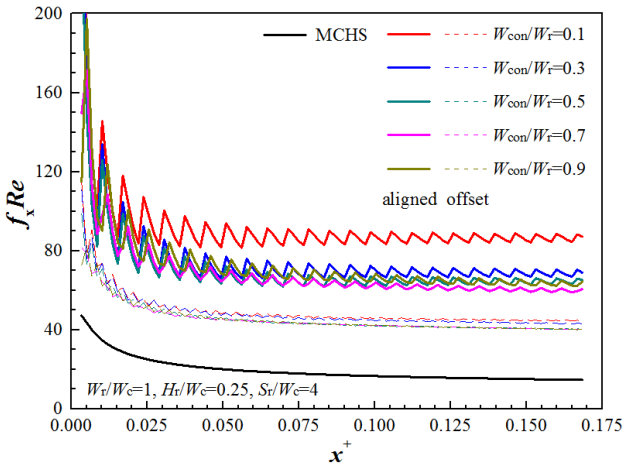
MCHS
$W_{con}/W_r$=0.1
$W_{con}/W_r$=0.3
$W_{con}/W_r$=0.5
$W_{con}/W_r$=0.7
$W_{con}/W_r$=0.9
aligned offset
$W_r/W_c$=1, $H_r/W_c$=0.25, $S_r/W_c$=4
$f_x Re$
$x^+$
0
40
80
120
160
200
0.000
0.025
0.050
0.075
0.100
0.125
0.150
0.175

(a)

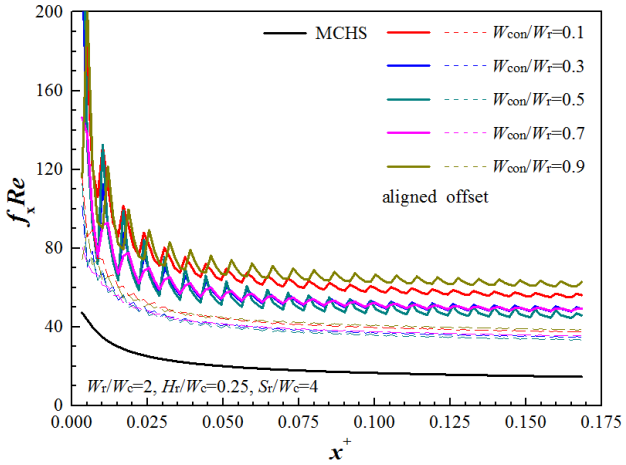
MCHS
$W_{con}/W_r$=0.1
$W_{con}/W_r$=0.3
$W_{con}/W_r$=0.5
$W_{con}/W_r$=0.7
$W_{con}/W_r$=0.9
aligned offset
$W_r/W_c$=2, $H_r/W_c$=0.25, $S_r/W_c$=4
$f_x Re$
$x^+$
0
40
80
120
160
200
0.000
0.025
0.050
0.075
0.100
0.125
0.150
0.175

(b)

Fig. 14

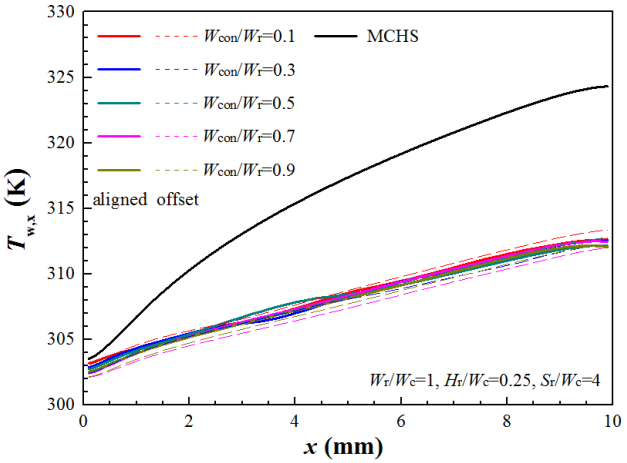
330
325
320
315
310
305
300
0
2
4
6
8
10
$T_{w,x}$ (K)
$x$ (mm)
$W_{con}/W_r$=0.1
$W_{con}/W_r$=0.3
$W_{con}/W_r$=0.5
$W_{con}/W_r$=0.7
$W_{con}/W_r$=0.9
MCHS
aligned offset
$W_r/W_c$=1, $H_r/W_c$=0.25, $S_r/W_c$=4

(a)

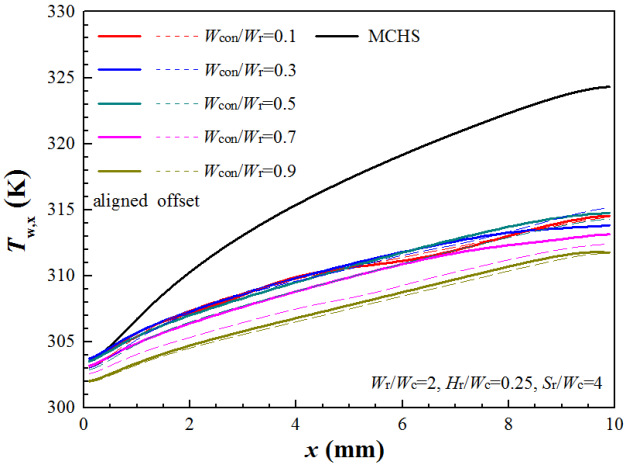
330
325
320
315
310
305
300
0
2
4
6
8
10
$T_{w,x}$ (K)
$x$ (mm)
$W_{con}/W_r$=0.1
$W_{con}/W_r$=0.3
$W_{con}/W_r$=0.5
$W_{con}/W_r$=0.7
$W_{con}/W_r$=0.9
MCHS
aligned offset
$W_r/W_c$=2, $H_r/W_c$=0.25, $S_r/W_c$=4

(b)

Fig. 15

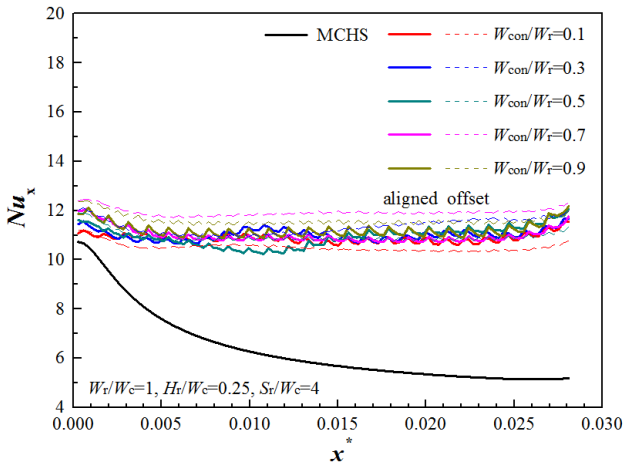
MCHS
$W_{con}/W_r$=0.1
$W_{con}/W_r$=0.3
$W_{con}/W_r$=0.5
$W_{con}/W_r$=0.7
$W_{con}/W_r$=0.9
aligned offset
$W_r/W_c$=1, $H_r/W_c$=0.25, $S_r/W_c$=4
$Nu_x$
$x^*$

(a)

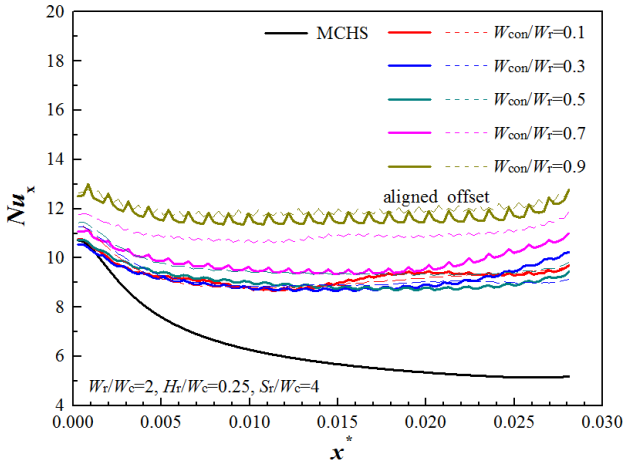
MCHS
$W_{con}/W_r$=0.1
$W_{con}/W_r$=0.3
$W_{con}/W_r$=0.5
$W_{con}/W_r$=0.7
$W_{con}/W_r$=0.9
aligned offset
$W_r/W_c$=2, $H_r/W_c$=0.25, $S_r/W_c$=4
$Nu_x$
$x^*$

(b)

Fig. 16

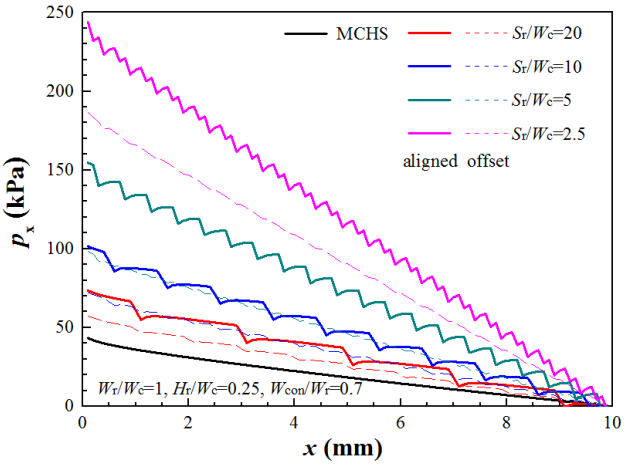
MCHS
$S_r/W_c$=20
$S_r/W_c$=10
$S_r/W_c$=5
$S_r/W_c$=2.5
aligned offset
$W_r/W_c$=1, $H_r/W_c$=0.25, $W_{con}/W_r$=0.7
$p_x$ (kPa)
$x$ (mm)
0
50
100
150
200
250
0
2
4
6
8
10

(a)

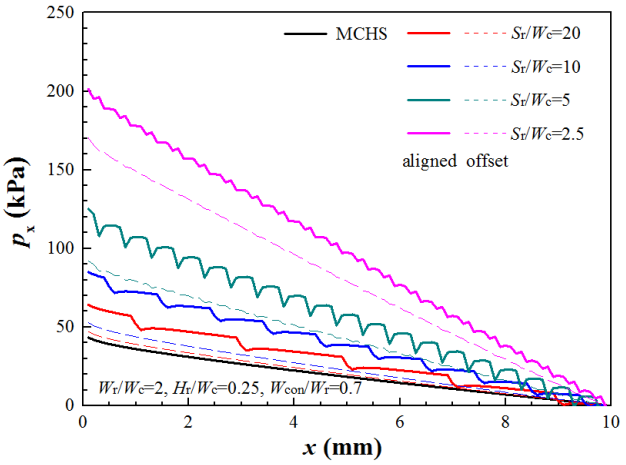
MCHS
$S_r/W_c$=20
$S_r/W_c$=10
$S_r/W_c$=5
$S_r/W_c$=2.5
aligned offset
$W_r/W_c$=2, $H_r/W_c$=0.25, $W_{con}/W_r$=0.7
$p_x$ (kPa)
$x$ (mm)
0
50
100
150
200
250
0
2
4
6
8
10

(b)

Fig. 17

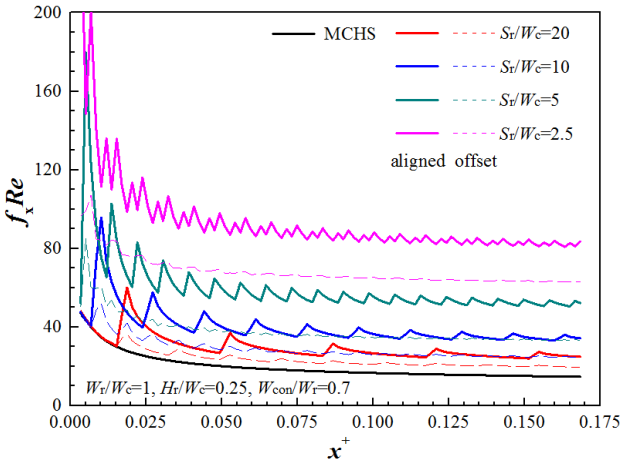
MCHS
$S_r/W_c$=20
$S_r/W_c$=10
$S_r/W_c$=5
$S_r/W_c$=2.5
aligned offset
$W_r/W_c$=1, $H_r/W_c$=0.25, $W_{con}/W_r$=0.7
$f_x Re$
$x^+$
0
40
80
120
160
200
0.000
0.025
0.050
0.075
0.100
0.125
0.150
0.175

(a)

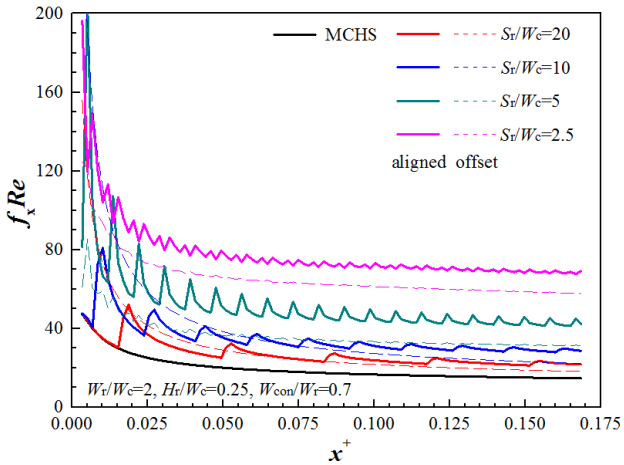
MCHS
$S_r/W_c$=20
$S_r/W_c$=10
$S_r/W_c$=5
$S_r/W_c$=2.5
aligned offset
$W_r/W_c$=2, $H_r/W_c$=0.25, $W_{con}/W_r$=0.7
$f_x Re$
$x^+$
0
40
80
120
160
200
0.000
0.025
0.050
0.075
0.100
0.125
0.150
0.175

(b)

Fig. 18

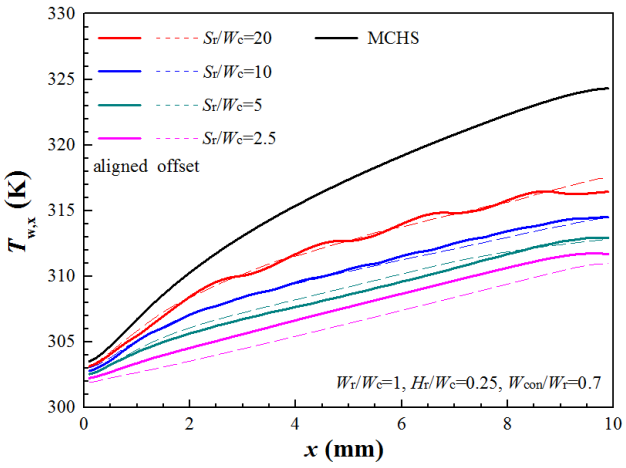
330
325
320
315
310
305
300
0
2
4
6
8
10
$T_{w,x}$ (K)
$x$ (mm)
$S_r/W_c$=20
$S_r/W_c$=10
$S_r/W_c$=5
$S_r/W_c$=2.5
MCHS
aligned offset
$W_r/W_c$=1, $H_r/W_c$=0.25, $W_{con}/W_r$=0.7

(a)

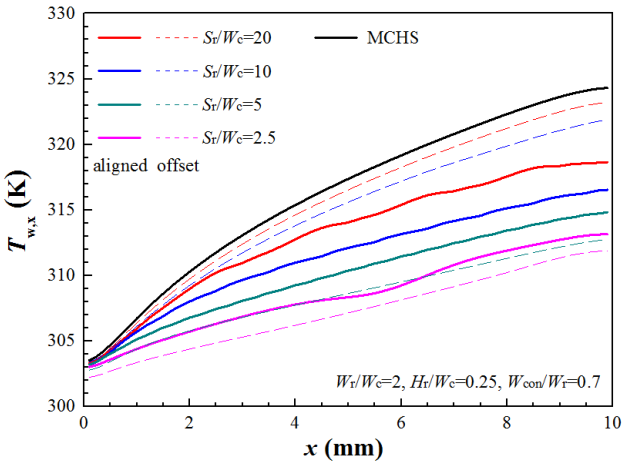
330
325
320
315
310
305
300
0
2
4
6
8
10
$T_{w,x}$ (K)
$x$ (mm)
$S_r/W_c$=20
$S_r/W_c$=10
$S_r/W_c$=5
$S_r/W_c$=2.5
MCHS
aligned offset
$W_r/W_c$=2, $H_r/W_c$=0.25, $W_{con}/W_r$=0.7

(b)

Fig. 19

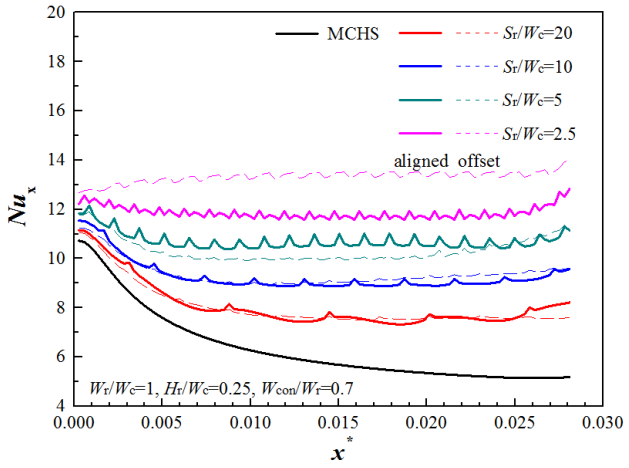
MCHS
$S_r/W_c$=20
$S_r/W_c$=10
$S_r/W_c$=5
$S_r/W_c$=2.5
aligned offset
$W_r/W_c$=1, $H_r/W_c$=0.25, $W_{con}/W_r$=0.7
$Nu_x$
$x^*$

(a)

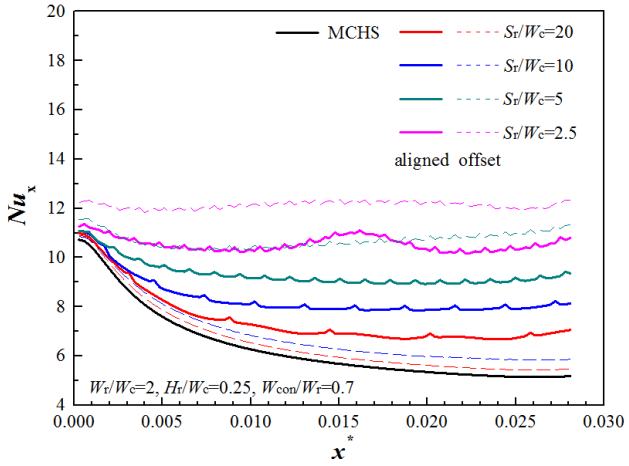
MCHS
$S_r/W_c$=20
$S_r/W_c$=10
$S_r/W_c$=5
$S_r/W_c$=2.5
aligned offset
$W_r/W_c$=2, $H_r/W_c$=0.25, $W_{con}/W_r$=0.7
$Nu_x$
$x^*$

(b)